Mathematical Models and Methods in Applied Sciences

Hysteresis and stop-and-go waves in traffic flows

Andrea Corli
Department of Mathematics and Computer Science, University of Ferrara
44121 Ferrara, Italy
andrea.corli@unife.it

Haitao Fan
Department of Mathematics, Georgetown University
Washington, DC 20057, USA
fan@math.georgetown.edu

Received (Day Month Year)
Revised (Day Month Year)
Communicated by (xxxxxxxxxx)

Stop-and-go waves, also called phantom jams, are often observed in real traffic flows but can be produced neither by the classical Lighthill-Whitham-Richards (LWR) model nor by its known variants. To capture stop-and-go waves, we add hysteresis to the LWR model. For the model we propose, all possible viscous waves are found, and necessary and sufficient conditions for their existence are provided. In particular, deceleration and acceleration shocks appear; the latter were never rigorously defined before, in spite of the fact that they were observed in real traffic flows. Stop-and-go waves can be constructed by a pair of deceleration and acceleration shocks that completes a hysteresis cycle, illustrating how hysteresis loops lead to stop-and-go waves. In contrast, in the phase region where anticipation (i.e., negative hysteresis) loops exist, stop-and-go waves are not present, and speed variations decay. Riemann solutions are then found for all possible Riemann data. We explicitly show that, in the phase region where hysteresis loops exist, a sufficient deviation in speed of a few vehicles in an otherwise uniform car platoon can generate stop-and-go waves, confirming observations of real traffic experiments.

Keywords: Hysteresis, traffic flow; stop-and-go; phantom jam; traveling wave; acceleration shock; Riemann solution.

AMS Subject Classification: 35L65, 35C07, 90B20

1. Introduction

The simplest macroscopic model for traffic flows is the famous Lighthill-Whitham-Richards (LWR) equation

$$\rho_t + (\rho v)_x = 0, \tag{1.1}$$

see Refs. 29 and 35, where ρ is the car density, and the velocity v is assumed to be a given function of ρ. Numerous works have been done on the LWR model and its

extensions, see the reviews Refs. 7, 17, the books Refs. 14, 15 and references cited therein.

Stop-and-go waves, where vehicles go through sequences of accelerations, decelerations and stops, are typical of congested traffic flows and occur in daily life. Experiments done in Refs. 38 and 39 showed that stop-and-go waves can be generated by drivers' behavior alone.

It has been known since Refs. 29 and 35 that the LWR model cannot produce stop-and-go waves, especially when both fronts of a stop-and-go wave are sharp, see Refs. 7, 17, 32. This is because the two sharp fronts are shock waves: one of them connects a traffic state S_1 with a traffic state S_2 from upstream to downstream, while the other connects S_2 to S_1. Traffic models in the form of hyperbolic balance laws cannot produce both shocks because at least one of them will violate the Lax condition. Many attempts were made to fix deficiencies of LWR model by modifying LWR model in various ways, but none of them seems to produce stop-and-go waves explicitly. A recent attempt is proposed in Ref. 37, where the authors constructed jamiton solutions, resembling stop-and-go waves, for some traffic-flow models. A jamiton solution's slow segment has a fixed length and its acceleration front is smooth. However, numerous observations of stop-and-go waves in real traffic flows show that the acceleration front can be as sharp as the deceleration shock, and the slow segment's length can be arbitrary, see e.g. Fig. 3 in Ref. 27 showing observations of Refs. 8, 39, 41; see also Fig. 3 in Ref. 21 and Fig. 5a in Ref. 38. In summary, all known continuum traffic models disallow stop-and-go waves when both fronts of a stop-and-go wave are sharp.

In the existing literature, drivers' hysteresis behavior is often reported and hysteresis loops are believed to cause stop-and-go waves. More precisely, it is known that the density-speed relation $v = v^A(\rho)$ in acceleration may differ from the analogous relation $v = v^D(\rho)$ in deceleration, see Refs. 33, 34, 41, 42, 43, 45. It is known as well that it may happen either $v^A(\rho) > v^D(\rho)$ or $v^A(\rho) < v^D(\rho)$, according to the ranges of the density, and that the difference $|v^A - v^D|$ is small for low densities, see Fig. 3 in Ref. 7. In general, the difference $|v^A - v^D|$ is related to hysteresis. This was first noticed for real-world data in Ref. 41, where a behavior as in Fig. 1 was first observed. Such a behavior was explained through a mathematical model in Ref. 45. According to Ref. 45, when the density is low, drivers *react by anticipation*, and this results in the counterclockwise anticipation loop ℓ_-. When the density is high, drivers' *delay in reaction* (hysteresis) is a more significant factor, resulting in the clockwise hysteresis loop ℓ_+. Reacting on anticipation is the opposite of reacting with delay; the anticipation loop ℓ_- is also called negative hysteresis loop. Several other papers deal with hysteresis in traffic flows, see for instance Refs. 2, 3, 4, 5, 6, 7, 12, 27, 28, 36, 42, 43.

In the macroscopic fluid-dynamics models quoted above, hysteresis is never built in; sometimes it is deduced as a consequence of a linear approximation of the velocity around an equilibrium speed-density relation $v_e(\rho)$, see Ref. 45. On the other hand, microscopic models are flexible enough to include various drivers' behaviors for

each vehicle; however, the wave analysis is harder to perform due to the size of the systems.

In this paper, we prove that hysteresis causes stop-and-go waves via a macroscopic model. Our system differs from the LWR equation just for hysteresis; since the LWR model cannot produce stop-and-go waves but our model does, this shall prove our claim.

To introduce hysteresis into the LWR model, we take the shape of the speed-density relation shown in Fig. 1 for granted (see Fig. 3 of Ref. 41 and Figs. 8 and 9 of Ref. 45) and build the fundamental diagram from it. This way, the range of speeds corresponding to the same density is as wide as suggested by numerous observations of real traffic, see e.g. Fig. 3 in Ref. 7. The presence of different loops in the fundamental diagram gives us a setup to investigate how their rotation directions affect the existence of stop-and-go waves. The resulting 2×2 system, which is nonconservative and with discontinuous coefficients, is introduced in Sections 2 and 3 in Eulerian and Lagrangian coordinates, respectively.

In Section 4, we find all possible basic waves, especially viscous shocks, of the model. This is the necessary step to take not only for constructing Riemann solutions, but also for finding an appropriate definition of weak solutions for the model because, as suggested by Ref. 11, solutions of nonconservative hyperbolic systems are sensitive to the shape of viscous profiles of shocks. Among the basic waves of the model we find deceleration and acceleration shocks, and establish necessary and sufficient conditions for their existence. Acceleration shocks have never been previously pointed out, but they can be observed in existing data, see Fig. 3 in Ref. 21, serving as acceleration fronts of slow segments of stop-and-go waves. It is found that the end states of these viscous shock waves are essentially insensitive to the particular form of the viscosity.

In Section 5, a numerical scheme is proposed, which is tested to verify that it

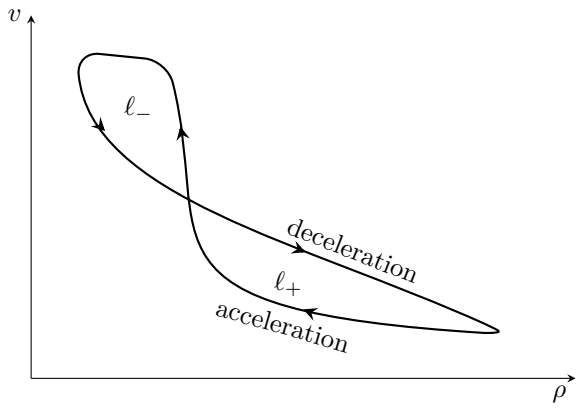

Fig. 1. An eight-loop figure with a positive subloop ℓ_+ and a negative subloop ℓ_-.

produces the right waves given in Section 4. One classical difficulty of numerical computation of solutions to partial differential equations with discontinuous coefficients is how to handle the product of a jump discontinuity and a delta function. In addition, shocks of non-conservative hyperbolic systems are sensitive to the form of viscosity and hence to the numerical viscosity arising from the discretization. The upwinding scheme we propose avoids to handle these difficulties by using the structure of shock profiles obtained in Section 4.

In a recent paper, see Ref. 13, a definition of weak solution for the model proposed here is given for piecewise C^1 solutions, in the framework of Ref. 11. In particular, the numerical scheme proposed in Section 5 is shown there to be TVD (total variation diminishing). Moreover, the limit of a convergent subsequence generated by the approximation scheme is shown to satisfy the definition of weak solution of the model if the limit is piecewise C^1. Maximum and minimum principles for the speed and the hysteresis variable are also proved in Ref. 13.

In Section 6, we construct a set of "rational" Riemann solutions for all possible Riemann initial data, using the basic waves found in Section 4. The numerical scheme presented in Section 5 also produces this set of Riemann solutions. However, Riemann solutions of the model are not unique, because drivers can and do drive "irrationally". The model has other Riemann solutions to accommodate these drivers, as a traffic model should do.

In Section 7, the results obtained in the previous sections are used to study stop-and-go waves. It turns out that a steady-shaped stop-and-go solution can be constructed by a pair of deceleration and acceleration shocks that completes a positive hysteresis loop. This shows how hysteresis loops cause stop-and-go waves. Furthermore, we show that steady-shaped stop-and-go waves are impossible in the region of the fundamental diagram where anticipation loops occur. The formation and decay of traffic jams are investigated by considering the initial value problems of the model, where the piecewise-constant initial data simulate a few cars whose speeds differ from that of a uniform car platoon traveling on a long road. Car platoons traveling on a ring road can be simulated using periodic boundary condition. The solution corresponding to these initial values shows that in the region where there are hysteresis loops, a sufficient deviation in speed generates stop-and-go waves, echoing experiments in Refs. 38, 39. We also numerically verify that oscillations in speed decay in the region where anticipation loops (i.e., negative hysteresis loops) are present. This further demonstrates the role of hysteresis in traffic jams.

In the last Section 8, we investigate the effects of *small* variations in the speed. The examples there suggest another mechanism for the formation of traffic jams, that we describe as follows. While the overall speed $\bar{v}$ of a platoon is determined by the leading vehicle, vehicles inside a platoon can temporarily move slightly faster or slower than $\bar{v}$. Temporary overspeed of a vehicle results in tighter spacing for itself. If drivers are more likely to overspeed than to downspeed, then the platoon becomes more and more compact. Once the platoon is dense enough, a downspeed by one vehicle creates an expanding slower segment upstream. This process repeats

itself inside the slow segment to create an even slower segment upstream. Given enough time, this overspeed bias can cause traffic jams.

2. The model in Eulerian coordinates

It has been recognized since Ref. 33 that the speed-density relations corresponding to accelerations and decelerations are usually different. We denote these relations by $v = v^A(\rho)$ and $v = v^D(\rho)$, respectively. By a careful analysis of the data in Ref. 41, it was deduced in Ref. 45 that the curve $v = v^A(\rho)$ lies *above* the curve $v = v^D(\rho)$ in the (ρ, v)-plane when the density ρ is low, and vice versa when ρ is large. The reasoning is based on a few assumptions including *a):* drivers respond only to front stimuli, *b):* there is a velocity $v = v_e(\rho)$ that drivers keep whenever possible. The arguments in Ref. 45 are roughly as follows. When ρ is low, drivers have sufficient spacing ahead to drive basing on anticipation. In this case one has $v \sim v_e - \tau\rho(v_e')^2\rho_x$, see (7) in Ref. 45. As a consequence, at the same density, the speed v is higher than v_e in acceleration mode and lower than v_e in deceleration mode. On the contrary, when ρ is large one has $v \sim v_e - \tau\dot{v}$, see (9) in Ref. 45, which implies that v is lower than v_e for acceleration and higher than v_e for deceleration; see Fig. 1. Here, the dot denotes the *material derivative*,

$$\frac{\mathrm{d}w}{\mathrm{d}t} = \dot{w} := w_t + vw_x.$$

Between the two above extremes of density, the possibility of multiple intersections between the acceleration and deceleration curves is not ruled out, see Refs. 27 and 45.

Experimental data, see Fig. 3 in Ref. 7, support the existence of $v_e(\rho)$ for low ρ. When ρ is large, vehicles' speeds shown in Fig. 3 of Ref. 7 are scattered wide enough to put doubt on the existence of such a $v_e(\rho)$ for large ρ.

To study how the curve shown in Fig. 1 and the wide scattering of velocity for the same large ρ affect traffic flows, we take this shape for granted and idealize the fundamental diagram as in Fig. 2. A vehicle's state (ρ, v) lies in the region Ω bounded by the curves $v = v^A(\rho)$ and $v = v^D(\rho)$ in the first quadrant of the (ρ, v)-plane, see Fig. 2. With this fundamental diagram, we allow the flexibility of disregarding the existence of $v_e(\rho)$, without loosing the possibility of assigning both $v^D(\rho)$ and $v^A(\rho)$ as $v_e(\rho)$, if so desired. While both positive and negative loops can happen in a range of densities depending on the proportion of timid and aggressive drivers, see Ref. 27, for definiteness and simplicity we restrict them in disjoint ranges of ρ. We emphasize that this paper does not intend to favor one fundamental diagram over another, but to investigate the effects of hysteresis and the shape of a fundamental diagram on traffic flows.

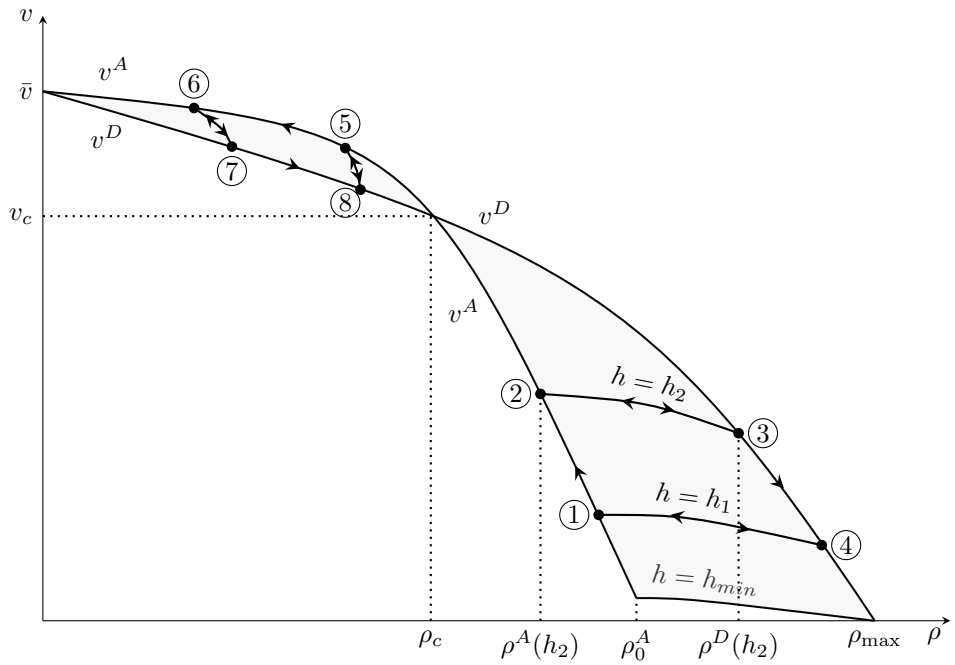

Fig. 2. The functions $v^A(\rho)$ and $v^D(\rho)$ and two scanning curves with $h_1 < h_2$. Arrows indicate the directions in which a car's state can move. A vehicle's state lies in the closed set Ω bounded by $v = v^A(u)$, $v = v^D(u)$, $\rho = 0$ and $v = 0$. The rotation directions of the hysteresis loops ①②③④① and ⑤⑥⑦⑧⑤ are dictated by the allowed directions on $v^A(\rho)$ and $v^D(\rho)$. The different rotation directions of the two loops provide a setting to study their effect on traffic flows.

Acceleration and deceleration curves The curves $v^A(\rho)$ and $v^D(\rho)$ are called *acceleration* and *deceleration curves*, respectively. We assume

$$v_\rho^A(\rho) < 0 \quad \text{and} \quad v_\rho^D(\rho) < 0, \tag{2.1}$$

$$\begin{aligned} &v = v^A(\rho) \text{ and } v = v^D(\rho) \text{ intersect only at } (\rho_c, v_c) \text{ (apart from } (0, \bar{v})); \\ &\text{their relative positions are as in Fig. 2.} \end{aligned} \tag{2.2}$$

Basing on Refs. 33, 41, 43, 45, a vehicle's state can move along $v = v^A(\rho)$ (or $v = v^D(\rho)$) only when accelerating (or decelerating). For example, if a vehicle's state is at the point ① in Fig. 2 and the density *in front of it* is decreasing, so $\dot{\rho} < 0$ and it accelerates, then its state moves along the curve $v = v^A(\rho)$ towards the point ②. Similarly, if a vehicle's state is at the point ③ in Fig. 2 and it decelerates (and hence $\dot{\rho} > 0$), then its state moves along the curve $v = v^D(\rho)$ towards the point ④.

Scanning curves If the vehicle with state at the point ① in Fig. 2 decelerates, due to increasing density in front of it, then its state has to move towards the curve $v = v^D(\rho)$ along a transition curve ①④. If the density continues to increase, the vehicle's state reaches the point ④. Further deceleration takes then place along the

curve $v = v^D(\rho)$. The shift from the acceleration to the deceleration regime (or vice versa) has been observed in Refs. 42, 43 to take place along curves, which we call *scanning curves*, see Ref. 9. We assume

there is one and only one scanning curve through each point on the curve $v = v^A(\rho)$, which is transversal to $v = v^A(\rho)$ at that point, and the same holds for the curve $v = v^D(\rho)$; scanning curves do not intersect. (2.3)

Some scanning curves are shown in Fig. 2 as ①④, ②③, ⑤⑧, ⑥⑦; they can be understood as a generalization of the coasting curves in Refs. 42, 43. As one sees from Fig. 2, there is a bottom scanning curve, namely the one through the point $(\rho_{\max}, 0)$. In that picture we assumed that it intersects the ρ axis at $\rho_{\max}$ only; in this way, cars stop only at the maximum density.

The region of physically meaningful (u, v)'s in Fig. 2 is the region enclosed by the curves $v = v^A(\rho)$, $v = v^D(\rho)$ and the lowest scanning curve. This region, defined by $\min h(x, t = 0) \le h \le \max h(x, t = 0)$, should be invariant for the model here proposed, as suggested by the results obtained in Refs. 13 and 9. Whether this is true is left for future research, as we do not need this result for this paper.

We parameterize the scanning curves with the *hysteresis parameter* h. A vehicle's state can move along scanning curves in both ways. Note that, as long as scanning curves can be observed, their identifying parameter h can be considered as observable. Since on each scanning curve the parameter h is constant, then a scanning curve can be written as $v = v^S(\rho, h)$. We assume

$$v^S_\rho(\rho, h) \le 0, \tag{2.4}$$

so that higher density usually results in lower speed.

We denote by $\rho^A(h)$ (or $\rho^D(h)$) the value of ρ at the intersection of the curves $v = v^S(\rho, h)$ and $v = v^A(\rho)$ (or $v = v^D(\rho)$). It follows immediately that

$$v^D(\rho^D(h)) = v^S(\rho^D(h), h), \quad v^A(\rho^A(h)) = v^S(\rho^A(h), h). \tag{2.5}$$

By (2.4) it also follows that

$$\rho^A(h) \le \rho^D(h). \tag{2.6}$$

Example 2.1 (Parametrization of scanning curves). By (2.3), through each point (ρ_0, v_0) on $v = v^D(\rho)$, there is a unique scanning curve. Let $h := \rho_0$ be the value of h for this scanning curve. This means to assign h as the ρ-coordinate of the intersection point between the curves $v = v^S(\rho, h)$ and $v = v^D(\rho)$; then $\rho^D(h) = h$. By (2.1), if $h_1 \ne h_2$ then $\rho^D(h_1) \ne \rho^D(h_2)$; thus, different scanning curves have different h's and the above parametrization is meaningful. Moreover, the function $\rho^D(h) = h$ is invertible, and its inverse function is $h^D(\rho) = \rho$.

The above example shows that we can require the parametrization to satisfy

$$\rho^D_h(h) > 0. \tag{2.7}$$

By (2.3), it is easily shown that this forces $\rho^A(h)$ to be an increasing function. Hence, we assume

$$\rho^A_h(h) > 0. \tag{2.8}$$

Then both $\rho^D(h)$, $\rho^A(h)$ have inverse functions, which are denoted as $h = h^D(\rho)$, $h = h^A(\rho)$, respectively. Then we define $h_c := h^A(\rho_c) = h^D(\rho_c)$. As a consequence, equality holds in (2.6) if and only if $h = h_c$. According to (2.7) and (2.8), we have

$$h^A_\rho(\rho) > 0 \quad \text{and} \quad h^D_\rho(\rho) > 0. \tag{2.9}$$

To visualize $h = h^D(\rho)$ in Fig. 2, fix a ρ_0 and draw the line $\rho = \rho_0$, intersecting $v = v^D(\rho)$ at (ρ_0, v_0). Then $h^D(\rho_0)$ is the h value of the scanning curve that intersects $v = v^D(\rho)$ at (ρ_0, v_0). The interpretation of $h = h^A(\rho)$ is analogous.

The meaning of $h^A(\rho)$ and $h^D(\rho)$ immediately implies that

$$v^A(\rho) = v^S(\rho, h^A(\rho)), \quad v^D(\rho) = v^S(\rho, h^D(\rho)). \tag{2.10}$$

Hysteresis loops The loops in Fig. 2 are called *hysteresis loops*. Since the relative position of the curves $v^A(\rho)$ and $v^D(\rho)$ changes, loop rotations in the ranges $\{\rho < \rho_c\}$ and $\{\rho > \rho_c\}$ are opposite.

We now collect in a formal way all assumptions above.

Assumption I.

(i) Functions $v^A(\rho), v^D(\rho)$ are defined over the interval $[0, \rho^A_0]$ and $[0, \rho_{max}]$ respectively with $v^A(\rho^A_0) \geq v^D(\rho_{max}) = 0$, $v^A(0) = v^D(0) = \bar{v}$. They are C^1 smooth and satisfy (2.1).

(ii) There is $\rho_c \in (0, \rho^A_0)$ so that $v^A(\rho) \geq v^D(\rho)$ for $\rho \leq \rho_c$ and $v^A(\rho) < v^D(\rho)$ for $\rho_c < \rho < \rho^A_0$.

(iii) Scanning curves form a one-parameter family of curves

$$\left\{(\rho, v^S(\rho, h))\right\}_{h \in [h_{min}, h_{max}]},$$

and provide a C^1 transversal foliation for the region Ω. The function v^S satisfies (2.4) *and* (2.6)*, while the parametrization satisfies* (2.7) *and* (2.8).

We define, in $[0, \rho_{\max}] \times [h_{\min}, h_{\max}]$, the velocity function

$$v = v(\rho, h) := \begin{cases} v^A(\rho) & \text{if } \rho \leq \rho^A(h), \\ v^S(\rho, h) & \text{if } \rho^A(h) < \rho < \rho^D(h), \\ v^D(\rho) & \text{if } \rho \geq \rho^D(h). \end{cases} \tag{2.11}$$

A driver's mode can then be classified as follows:

$$\begin{aligned} &\text{Acceleration mode:} && \dot{\rho}(x, \cdot) < 0 \text{ and } v = v^A(\rho); \\ &\text{Deceleration mode:} && \dot{\rho}(x, \cdot) > 0 \text{ and } v = v^D(\rho); \\ &\text{Scanning mode:} && v \text{ is between } v^A(\rho) \text{ and } v = v^D(\rho), \text{ and} \\ & && \text{neither in Acceleration nor Deceleration mode.} \end{aligned} \tag{2.12}$$

Define the corresponding sets A, D and S, recall (2.6), as

$$\begin{aligned}
A &= \left\{(x,t) \in \mathbb{R} \times \mathbb{R}_+ \colon \rho(x,t) = \rho^A\left(h(x,t)\right),\ \dot\rho(x,t) < 0\right\},\\
D &= \left\{(x,t) \in \mathbb{R} \times \mathbb{R}_+ \colon \rho(x,t) = \rho^D\left(h(x,t)\right),\ \dot\rho(x,t) > 0\right\},\\
S &= \left\{(x,t) \in \mathbb{R} \times \mathbb{R}_+ \colon (x,t) \notin A \cup D \ \text{ and } \ \rho^A\left(h(x,t)\right) \le \rho(x,t) \le \rho^D\left(h(x,t)\right)\right\}.
\end{aligned}$$

To describe a driver's state at a point (x,t), we use the variables $(\rho, h)(x,t)$. The hysteresis parameter $h(x,t)$ records the hysteresis mode the driver is in; hence, it should follow the driver and be updated as the driver's vehicle moves along the traffic. In other words, $h(x,t)$ records the scanning curve to take should the vehicle at (x,t) switch into the scanning mode. When a driver is in acceleration (or deceleration) mode, the corresponding parameter h should be updated as $h^A(\rho)$ or $h^D(\rho)$ along the vehicle path; in scanning mode, h should not change. Thus, the equation for h is

$$h_t + v h_x = \chi_A(x,t)\left(h^A(\rho)_t + v h^A(\rho)_x\right) + \chi_D(x,t)\left(h^D(\rho)_t + v h^D(\rho)_x\right), \quad (2.13)$$

where χ_A is the characteristic function of the set A and so on. By combining (1.1) and (2.13) we obtain the following system of equations:

$$\begin{cases} \rho_t + (\rho v)_x = 0, \\ h_t + v h_x = \chi_A(x,t)\left(h^A(\rho)_t + v h^A(\rho)_x\right) + \chi_D(x,t)\left(h^D(\rho)_t + v h^D(\rho)_x\right). \end{cases} \quad (2.14)$$

If we understand system (2.14) as a system of balance laws, then the eigenvalues of the conservative part are v and $v + \rho v_\rho$; by (2.1) they both are less than or equal to the vehicle velocity, as it should be because drivers only respond to front stimuli. Indeed, in the scanning zone system (2.14) is a Temple system, see Refs. 10, 40, as we pointed out in Ref. 9 for an analogous model.

The second equation of the system (2.14) can possibly involve products of discontinuous functions with delta functions. Such products heavily depend on the detailed shape of the profiles approximating the delta functions, which are the derivatives of the shock profiles for the system, as suggested by Ref. 11. Thus, first we have to study traveling waves for a viscous approximation of system (2.14), see (4.2) below in Lagrangian coordinates, from which a possible definition of weak solution for (2.14) can be inferred. Recently, in this framework, the authors of Ref. 13 provided a definition of weak solutions of (2.14), and showed that such weak solutions exist if they are piecewise C^1.

For the model (2.14), the hysteresis parameter h does not change in scanning mode. It can be changed by adding another item to the right side of $(2.14)_2$ (i.e., the second equation in (2.14); we use this notation also in the following). For example, if h is subject to random perturbations, then we can add on the right-hand side of $(2.14)_2$ a random term such as a white noise. These possibilities are left for future works.

3. The model in Lagrangian coordinates

Tracing vehicle paths gives the advantage of seeing traffic from drivers' point of view. This is why in this section we convert (2.14) to Lagrangian coordinates. Then we define the variable

$$y = \int_{-\infty}^{x} \rho(t, x')\, dx',$$

which turns out to be a car label. If $\rho > 0$, Eulerian coordinates and Lagrangian coordinates are equivalent. Under the transformation $(x, t) \to (y, t)$, the model (2.14) becomes

$$\begin{cases} u_t - v(u,h)_y = 0, \\ h_t = \chi_A(y,t) h^A(u)_t + \chi_D(y,t) h^D(u)_t, \end{cases} \tag{3.1}$$

where $u := 1/\rho$ represents the spacing between vehicles. Notice that, in Lagrangian coordinates, the *time* derivative w_t is the *material* derivative $\dot{w}$. For simplicity we assume $\rho_{\max} = 1$ so that $u \in [1, \infty)$. One advantage of using Lagrangian coordinates is that they give the driver's point of view, since each vehicle is characterized by a fixed y. In particular, the first equation just states the simple fact that how fast the spacing between two cars is increasing is equal to the difference of speeds of these two cars.

Since it is customary to use x as first coordinate, we substitute y for x in (3.1) to get

$$\begin{cases} u_t - v(u,h)_x = 0, \\ h_t = \chi_A(x,t) h^A(u)_t + \chi_D(x,t) h^D(u)_t. \end{cases} \tag{3.2}$$

To clarify notations in (3.2), we translate the relevant part of Section 2 into Lagrangian coordinates as follows.

The function $h(x, t)$ still denotes the hysteresis parameter in which the driver of x-th vehicle is at time t. Under this notation, we rewrite all previous functions v^A, v^D, v^S, v into the new variables to obtain $v^A(u)$, $v^D(u)$, $v^S(u, h)$, $v(u, h)$, with a slight abuse of notation. The functions corresponding to $\rho^A(h)$, $\rho^D(h)$, $h^A(\rho)$, $h^D(\rho)$ are transformed to $u^A(h)$, $u^D(h)$, $h^A(u)$, $h^D(u)$. If h is chosen as the u-coordinate of the intersection of the curves $v = v^D(u)$ and $v^S(u, h)$, then $h \in [1, \infty)$; for simplicity we keep this interval as the general range of h. Such an example of parametrization shows that we can require $u^D_h(h) > 0$. We refer to Fig. 3 and define

$$v = v(u,h) := \begin{cases} v^D(u) & \text{if } u \le u^D(h), \\ v^S(u,h) & \text{if } u^D(h) < u < u^A(h), \\ v^A(u) & \text{if } u \ge u^A(h), \end{cases} \tag{3.3}$$

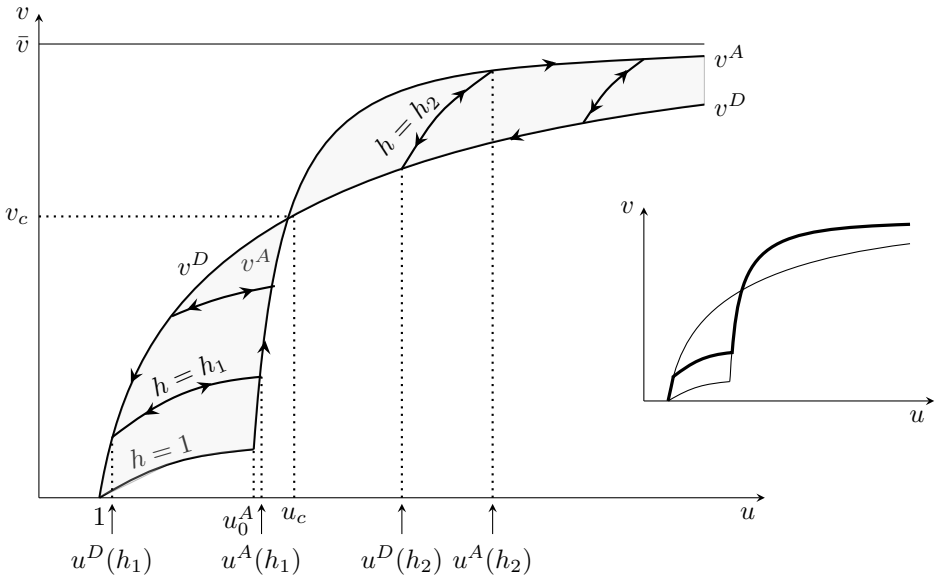

Fig. 3. The functions $v^A(u)$, $v^D(u)$ and two scanning curves with $h_1 < h_c < h_2$. Small on the right: the plot of the function $u \mapsto v(u, h_1)$ with a thick line.

where, with a slight abuse of notation,

$$A = \left\{(x,t) \in \mathbb{R} \times \mathbb{R}_+ \colon u(x,t) = u^A\left(h(x,t)\right),\ u_t(x,t) > 0\right\}, \tag{3.4}$$

$$D = \left\{(x,t) \in \mathbb{R} \times \mathbb{R}_+ \colon u(x,t) = u^D\left(h(x,t)\right),\ u_t(x,t) < 0\right\}, \tag{3.5}$$

$$S = \left\{(x,t) \in \mathbb{R} \times \mathbb{R}_+ \colon (x,t) \notin A \cup D \text{ and } u^A\left(h(x,t)\right) \geq u(x,t) \geq u^D\left(h(x,t)\right)\right\}.$$

The set of physical states (u, h)'s is the region denoted by

$$\Omega := \left\{(u,h) \in [1,\infty) \times [1,\infty)\ :\ u^D(h) \leq u \leq u^A(h)\right\}, \tag{3.6}$$

with some abuse of notations; for simplicity, we also denote with Ω the set of the physical states (u, v). In Lagrangian coordinates, Assumption (I) becomes, in a concise way,

Assumption (I′) The functions $v^A(u), v^D(u)$ and $v^S(u,h)$ are C^1, and the following conditions hold:

$$\begin{aligned}
&v^A_u > 0,\ v^D_u > 0,\ v^S_u(u,h) \geq 0;\\
&v^S(u,h_1) \neq v^S(u,h_2) \text{ if } h_1 \neq h_2;\\
&u^A(h) \geq u^D(h), \text{ with "=" if and only if } h = h_c;\\
&u^D_h > 0,\ u^A_h > 0,\ h^A_u > 0,\ h^D_u > 0.
\end{aligned} \tag{3.7}$$

Since the velocity v takes on different forms depending on modes, there could be possibilities for self-contradiction. For instance, at the intersection of scanning

and acceleration mode, if the sign of u_t calculated according to scanning mode and acceleration mode are different, then self-contradiction occurs. To avoid such contradictions, the signs of the functions v_u^A, v_u^D, v_u^S must be the same when the corresponding curves $v^A(u)$, $v^D(u)$, $v^S(u,h)$ intersect, i.e. these *compatibility conditions* must be required:

$$\begin{aligned} \operatorname{sign} v_u^A(u) &= \operatorname{sign} v_u^S(u,h) \quad && \text{when } h = h^A(u) \neq h_c, \\ \operatorname{sign} v_u^D(u) &= \operatorname{sign} v_u^S(u,h) \quad && \text{when } h = h^D(u) \neq h_c. \\ \operatorname{sign} v_u^D(u) &= \operatorname{sign} v_u^A(u) \quad && \text{when } h = h_c. \end{aligned}$$

Indeed, these conditions are implied by Assumption (I′).

By $(3.7)_1$, the quasilinear system (3.2) is hyperbolic, and its eigenvalues are

$$\lambda_1 = -[\chi_A v_u^A + \chi_D v_u^D + \chi_S v_u^S] = -v_u(u,h) \leq 0 \text{ and } \lambda_2 = 0. \tag{3.8}$$

Notice that the strict hyperbolicity is lost at points where $v_u^S(u,h) = 0$. When this happens, it is well-known that nonlinear resonance occurs, see Refs. 19, 20, 24, 25. In these cases, some explicit examples show that the total variation of the solution u can increase without bound, see Ref. 30. Furthermore, when constructing a solution with the Glimm scheme, the approximations may also have unbounded total variation as the discretization becomes small, see Ref. 40. In view of these facts, the stricter assumption $v_u^S > 0$ in (3.7) can make the analysis of the model easier.

4. Basic waves

In this section we find the shock and rarefaction waves for system (3.2). These basic waves are visible in experimental data, and hence can be used for at least qualitative validation. They are also needed in later sections for constructing solutions of (3.2), such as stop-and-go waves, and construct numerical schemes for (3.2).

A shock wave of (3.2) is a solution of the form

$$(u,h)(x,t) = \begin{cases} (u_-, h_-) & \text{if } x - st < 0, \\ (u_+, h_+) & \text{if } x - st > 0, \end{cases} \tag{4.1}$$

where $(u_\pm, h_\pm)$ are constants and s is the shock speed, see Ref. 10. Typically, a shock wave is required to have a viscous profile derived from the corresponding viscous system

$$\begin{cases} u_t - v(u,h)_x = \epsilon \left(B(u)u_x\right)_x, \\ h_t = \chi_A(x,t)h^A(u)_t + \chi_D(x,t)h^D(u)_t, \end{cases} \tag{4.2}$$

where $B(u) > 0$ is assumed to be smooth and bounded away from 0. Such a viscosity form can be argued as rational as follows. Recall that $v(u,h)$ is the equilibrium speed. In the non-equilibrium situation where $u_x > 0$ (or $u_x < 0$), the driver of the x-th vehicle sees that the spacing is sparser (or denser) the further down the road;

as a consequence, he/she anticipates that his/her speed will be faster (or slower), and he/she can drive a little faster (or slower) than otherwise at the speed of

$$v = v(u,h) + \epsilon B(u)u_x.$$

Plugging this into the conservation law $u_t - v_x = 0$ yields Eq. $(4.2)_1$. We have not found a rational reason to add a diffusion term such as h_{xx} to $(4.2)_2$. The driver at x cannot observe *directly* the hysteresis states of drivers nearby, nor he/she has much reason to act according to them. Instead, the driver at the point x senses the h of nearby drivers through their (u,v) values, and such diffusion process is already covered by the diffusion item of u_{xx} form through $(4.2)_1$.

Solutions of (3.2) are usually defined as $\epsilon \to 0+$ limits of solutions to (4.2), if the limits exist. Readers shall see that results of this paper are independent of $B(u)$, as long as B is smooth, positive, and bounded away from zero, as we assume. The equations for the viscous profile $(u,h)(x,t) = (u,h)((x-st)/\epsilon)$ of a shock wave connecting two states (u_-,h_-) and (u_+,h_+) with $u_- \neq u_+$ are

$$\begin{cases} Bu' = -s(u-u_\pm) - (v-v_\pm), \\ sh' = s\chi_A(\xi)\left(h^A(u)\right)' + s\chi_D(\xi)\left(h^D(u)\right)', \\ (u,h)(\pm\infty) = (u_\pm,h_\pm),\ (u',h')(\pm\infty) = (0,0), \end{cases} \tag{4.3}$$

where $' = \frac{\mathrm{d}}{\mathrm{d}\xi}$ for $\xi = (x-st)/\epsilon$. The jump condition dictates the speed of the shock wave as

$$s = -\frac{v(u_+,h_+) - v(u_-,h_-)}{u_+ - u_-}. \tag{4.4}$$

With respect to the variable ξ, the sets A and D in (3.4), (3.5) become

$$A = \left\{\xi \in \mathbb{R}\colon su'(\xi) < 0 \text{ and } u(\xi) = u^A\left(h(\xi)\right)\right\}, \tag{4.5}$$

$$D = \left\{\xi \in \mathbb{R}\colon su'(\xi) > 0 \text{ and } u(\xi) = u^D\left(h(\xi)\right)\right\}. \tag{4.6}$$

For simplicity we kept the same notation as in (3.4), (3.5).

Remark 4.1. When $s \neq 0$, we look for solutions of (4.3) in $C(\mathbb{R},\mathbb{R}^2)$. If they exist, then $u(\xi)$ is C^1 while $h'(\xi)$ is bounded in view of (4.3). When $s = 0$, Eq. $(4.3)_2$ is trivially satisfied and both $h(\xi)$ and $u'(\xi)$ can have jump discontinuities.

In the following, we make the Assumption (I'), see (3.7).

Our first result shows that shock waves cannot travel forwards relative to vehicles, a minimum requirement for traffic models.

Theorem 4.1. *There is no solution to* (4.3) *with* $s > 0$.

Proof. It suffices to show that if (4.3) has a solution $(u,h)(\xi)$ and $s \neq 0$, then $s < 0$. To this end, rewrite $(4.3)_1$ as

$$Bu' = (u-u_-)\left[-s - \frac{v-v_-}{u-u_-}\right]. \tag{4.7}$$

For $u(\xi)$ to leave u_- as ξ increase from $-\infty$, a necessary condition is

$$\lim_{\xi\to-\infty}\left[-s-\frac{v-v_-}{u-u_-}\right]\geq 0. \tag{4.8}$$

The limit can be calculated as

$$\lim_{\xi\to-\infty}\frac{v-v_-}{u-u_-}=\lim_{\xi\to-\infty}\frac{v'}{u'}=v_u(u_-,h_-)+\chi(S)v_h^S(u_-,h_-)\frac{h'}{u'}=v_u(u_-,h_-)\geq 0,$$

and hence $s\leq 0$. In the above calculation the continuity of $v(u,h)$ is used to cancel out the delta functions resulted from the derivatives of χ_A,χ_S and χ_D. If $s\neq 0$, then $s<0$ holds. □

The following lemma is analogous to Lemma 4.1 in Ref. 9. We provide here a different proof, which in turn is often used in the proofs of later results.

Lemma 4.1. *Assume $u_-\neq u_+$ and let* (4.3) *have a continuous solution (u,h) with $s\neq 0$. Then*

(i) u' is continuous and never vanishes, hence u is strictly monotone;
(ii) h is Lipschitz-continuous and monotone with the same type of monotonicity of u.

Proof. First, we prove *(i)*. By Remark 4.1, if $s\neq 0$ then u' is required to be continuous, h' is bounded and hence h is Lipschitz-continuous. Assume, for contradiction, that there is a point ξ_0 where $u'(\xi_0)=0$, implying $h'(\xi_0)=0$ by $(4.3)_2$ since $s\neq 0$. Then, equations $(4.3)_{1,2}$ have the constant solution $\big(\bar u(\xi),\bar h(\xi)\big)\equiv(u(\xi_0),h(\xi_0))$. We claim that this is the *only* solution of $(4.3)_{1,2}$ and thus violates $(4.3)_3$. This claim requires a proof since the standard uniqueness of solutions to initial value problems for ordinary differential equations does not apply here since the right-hand side of $(4.3)_2$ is discontinuous. To prove this claim, assume on the contrary that there is also a non-constant solution $(u,h)(\xi)$ to $(4.3)_{1,2}$ satisfying $u'(\xi_0)=0$. Since $u'(\xi)$ is continuous and $u(\xi)$ is not a constant function, the set

$$\{\xi\in\mathbb{R}\ :\ u'(\xi)=0\}$$

cannot be dense in $\mathbb{R}$. Then, the point ξ_0 can be further selected so that

$$u'(\xi)\neq 0\quad\forall\xi\in(\xi_0,\xi_0+\nu), \tag{4.9}$$

for some $\nu>0$. Because $u'(\xi_0)=0$, we have

$$-s\,(u(\xi_0)-u_-)-v(u,h)(\xi_0)+v_-=Bu'(\xi_0)=0.$$

With this, the equations $(4.3)_{1,2}$ can be rewritten as

$$\begin{cases} B(u)(u-u_0)'=-s(u-u_0)-(v(u,h)-v_0)\,,\\ (h-h_0)'=\big[\chi_A h_u^A+\chi_D h_u^D\big]\,(u-u_0)', \end{cases} \tag{4.10}$$

where $(u_0, h_0, v_0) := (u, h, v(u,h))(\xi_0)$. Eq. $(4.10)_2$ yields

$$h(\xi) - h_0 = O(1)(u(\xi) - u_0), \qquad \xi \in (\xi_0, \xi_0 + \nu). \tag{4.11}$$

Notice that $(u(\xi) - u_0)' \neq 0$ for $\xi \in (\xi_0, \xi_0 + \nu)$ by (4.9), and $B(u) > \mu > 0$ for a constant $\mu > 0$. Then the estimate

$$\left| \int_{\xi_0}^{\xi} B\left(u(\zeta)\right) \left[u(\zeta) - u_0\right]' d\zeta \right| \geq \mu |u(\xi) - u_0| \tag{4.12}$$

holds for any $\xi \in (\xi_0, \xi_0 + \nu)$. By integrating $(4.10)_1$ and using (4.11), (4.12) we deduce

$$\mu |u(\xi) - u_0| \leq \nu O(1) \max_{\xi_0 < \zeta \leq \xi_0 + \nu} |u(\zeta) - u_0|, \quad \forall \xi \in (\xi_0, \xi_0 + \nu). \tag{4.13}$$

Since $\nu > 0$ can be arbitrarily small, this infers that $u(\xi) \equiv u_0$ for $\xi \in (\xi_2, \xi_2 + \nu)$, and hence $h(\xi) \equiv h_0$, for all $\xi \in (\xi_0, \xi_0 + \nu)$. This, however, violates (4.9). This contradiction establishes the claim.

The statement *(ii)* follows immediately from $(4.3)_2$ and $(3.7)_4$. □

Remark 4.2. Notice that although $u(\xi)$ is strictly monotone, the monotonicity of $h(\xi)$ may not be strict.

4.1. *Stationary shocks*

These shocks have zero speed; the equations for the profiles are given by (4.3) with $s = 0$ and $v_- := v(u_-, h_-) = v(u_+, h_+) =: v_+$ by (4.4).

Theorem 4.2. *Consider two states $(u_\pm, h_\pm) \in \Omega$ such that $v_- = v_+$. Then system (4.3) has infinitely many solutions with $s = 0$ connecting (u_-, h_-) to (u_+, h_+).*

Proof. When $s = 0$, the system (4.3) is reduced to

$$\begin{cases} Bu' = -v(u,h) + v_-, \\ (u,h)(\pm\infty) = (u_\pm, h_\pm)\,. \end{cases} \tag{4.14}$$

If $u_- > u_+$, we select $h = h(u)$ in such a way that, see Fig. 4,

$$h_\pm = h\left(u_\pm\right) \quad \text{and} \quad v\left(u, h(u)\right) > v_- \quad \text{for } u \in (u_+, u_-). \tag{4.15}$$

Then the unstable trajectory issued from the equilibrium point (u_-, h_-) and entering into the region $\{u < u_-\}$ will continue to decrease as ξ increases, until it enters another equilibrium point (u_+, h_+) at $\xi = \infty$. Then $(u(\xi), h(u(\xi)))$ is indeed a solution to (4.15).

If $u_- < u_+$, the proof is analogous but choosing $h = h(u)$ such that $v\left(u, h(u)\right) < v_-$ in (4.15). □

We notice that this result is obvious inside the scanning zone, since system (3.2) has 0 as a (linearly degenerate) eigenvalue. In this case, stationary shocks are nothing else than contact discontinuities.

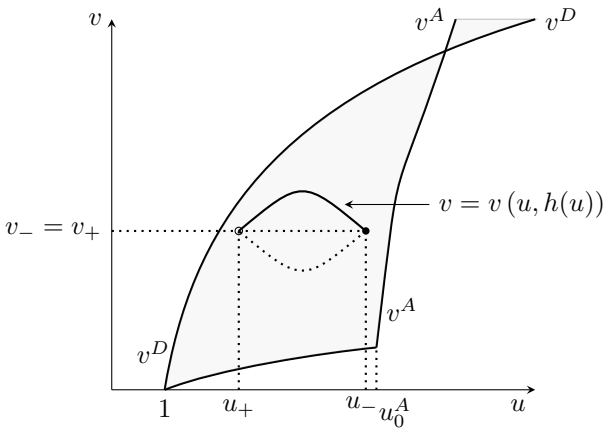

Fig. 4. States (u_-, v_-) and $(u_+, v_+ = v_-)$ can be connected by a stationary shock.

4.2. *Scanning to acceleration or deceleration shocks*

In this section we focus on shock waves connecting a state on a scanning curve with a state located either on the acceleration curve or on the deceleration curve. We refer to Fig. 5.

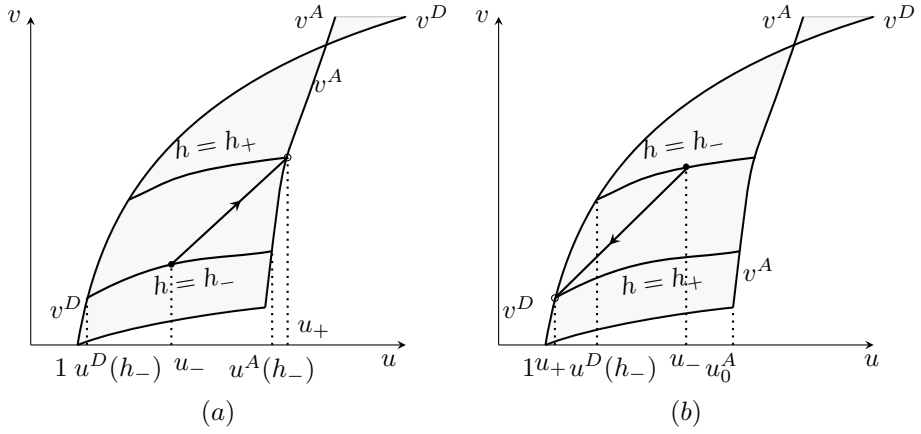

Fig. 5. (a): An acceleration shock, and (b): a deceleration shock connecting states (v_-, h_-) and (v_+, h_+).

Theorem 4.3. *Assume* $(u_\pm, h_\pm) \in \Omega$ *and* $h_- < h_+$ *The necessary and sufficient*

condition for (4.3) *to have a solution with* $s < 0$ *is*

$$\begin{cases} u_- < u_+ = u^A(h_+), \quad \textit{and} \\ \dfrac{v_+ - v_-}{u_+ - u_-} > \dfrac{v(u,h_-) - v_-}{u - u_-} \quad \textit{for } u_- < u < u_+. \end{cases} \tag{4.16}$$

The solution is unique, up to a shift in ξ*, and its structure is*

$$u'(\xi) > 0 \quad \textit{and} \quad h(\xi) = \begin{cases} h_- & \textit{if } \xi < \xi_1, \\ h^A\left(u(\xi)\right) & \textit{if } \xi \geq \xi_1. \end{cases} \tag{4.17}$$

for some $\xi_1 \in \mathbb{R}$ *such that* $u(\xi_1) = u^A(h_-)$.

Proof. We refer to Fig. 5*(a)*. First, we show that (4.16) is *sufficient* for (4.3) to have a solution with $s < 0$.

Because $h_- < h_+$, we have $u_- \leq u^A(h_-) < u^A(h_+) = u_+$ by $(3.7)_4$ and

$$v_- = v^S(u_-, h_-) \leq v^S\left(u^A(h_-), h_-\right) = v^A\left(u^A(h_-)\right)$$

by Assumption (I′), $(3.7)_1$. Combining this with (4.4), we obtain

$$s = \frac{v_- - v_+}{u_+ - u_-} \leq \frac{v^A(u^A(h_-)) - v^A(u_+)}{u_+ - u_-} < 0. \tag{4.18}$$

When the condition $(4.16)_2$ holds, the equation

$$Bu' = (u - u_-)\left[-s - \frac{v(u,h_-) - v_-}{u - u_-}\right] \tag{4.19}$$

has an increasing solution $u = u(\xi)$ with $u(\pm\infty) = u_\pm$, because the solution of (4.19) with any initial value $u(0) \in (u_-, u_+)$ is increasing and goes into equilibrium u_-, u_+ as $\xi \to \pm\infty$ respectively. Define

$$h(u) = \begin{cases} h_- & \text{if } u \in \left[u_-, u^A(h_-)\right], \\ h^A(u) & \text{if } u \in \left[u^A(h_-), u_+\right]. \end{cases} \tag{4.20}$$

Then $(u,h) := (u(\xi), h(u(\xi)))$ satisfies $(4.3)_1$, because $v\left(u(\xi), h(\xi)\right) = v\left(u(\xi), h_-\right)$ and hence makes Eq. (4.19) the same as $(4.3)_1$. To see that it also satisfies $(4.3)_2$, we notice that when ξ increases from $-\infty$, the pair $(u,h)(\xi)$ moves along the scanning curve $v = v^S(u, h_-)$ until some point $\xi = \xi_0$ where $u(\xi_0) = u^A(h_-)$. Eq. $(4.3)_2$ is trivially satisfied for $\xi \in (-\infty, \xi_0)$. Over the interval $\xi \in (\xi_0, \infty)$, we have $(u,h)(\xi) = \left(u, h^A(u)\right)(\xi)$ and $u' > 0$ by Lemma 4.1; hence $\chi_A = 1$ holds by (4.6), making Eq. $(4.3)_2$ satisfied. At the point $\xi = \xi_0$ where the two parts join, the pair $(u,h)(\xi)$ is continuous. Thus, $(4.3)_2$ is satisfied for all $\xi \in (-\infty, \infty)$.

Now, we show that (4.16) is also *necessary* for (4.3) to have a solution with $s < 0$. To show that $u_+ = u^A(h_+)$, we first notice that $u_+ \leq u^A(h_+)$ because $(u_+, h_+) \in \Omega$, see (3.6). Since $h_- < h_+$, for any subinterval $(h_1, h_2) \subset (h_-, h_+)$, there is a point $\xi_0 \in \mathbb{R}$ such that

$$h(\xi_0) \in (h_1, h_2) \quad \text{and} \quad h'(\xi_0) > 0.$$

By $(4.3)_2$ and $s < 0$, we have

$$0 < h'(\xi_0) = \left[\chi_A h_u^A + \chi_D h_u^D\right]_{|\xi=\xi_0} u'(\xi_0),$$

inferring that $u'(\xi_0) > 0$ by $(3.7)_4$ and hence we have either $\xi_0 \in A$ or $\xi_0 \in D$. By (4.6) and $s < 0$ we deduce $\xi_0 \in A$, and hence $u(\xi_0) = u^A\left(h(\xi_0)\right)$. Assume, for contradiction, that $u_+ < u^A(h_+)$. The arbitrariness of $h_1, h_2 \in (h_-, h_+)$ implies that the point $\xi_0 \in \mathbb{R}$ can be chosen so that $u_+ < u(\xi_0) = u^A\left(h(\xi_0)\right) \le u^A(h_+)$. Since $u_- < u^A(h_-) < u^A(h_+)$ because of $h_- < h_+$ and $(3.7)_4$, the estimate

$$\max\{u_+, u_-\} < u(\xi_0) = u^A\left(h(\xi_0)\right) \le u^A(h_+)$$

is true. Then, $u(\xi)$ is not monotone, violating Lemma 4.1. This contradiction proves $u_+ = u^A(h_+)$.

The necessity of $(4.16)_2$ can be argued as follows: Because of $u_- < u^A(h_-) < u^A(h_+) = u_+$ and Lemma 4.1, it follows that $u'(\xi) > 0$ for all $\xi \in \mathbb{R}$. Then, there is a point $\xi_1 \in \mathbb{R}$ so that $u(\xi) < u^A(h_-)$ for $\xi < \xi_1$, and $u(\xi) \ge u^A(h_-)$ for $\xi \ge \xi_1$. From Eq. $(4.3)_2$, we have $h(\xi) \equiv h_-$ for $\xi \le \xi_1$. Assume, for contradiction, that $(4.16)_2$ fails for some $u_2 \in (u_-, u_+)$. There is a $\xi_2 \in \mathbb{R}$ such that

$$u(\xi_2) = u_2, u'(\xi_2) > 0.$$

If $u_2 \in (u_-, u^A(h_-)]$, then $(4.3)_2$ implies $h(\xi_2) = h_-$. However, because $(4.16)_2$ fails at $u = u_2$, $(4.3)_1$ infers $u'(\xi_2) \le 0$, a contradiction. Note that $\xi \in A$ as ξ increases from $\xi = \xi_1$, and hence we have both $h(\xi) \ge h^A\left(u(\xi)\right) > h_-$ and

$$v(u,h)(\xi) = v\left(u(\xi), h^A(u(\xi))\right) = v^A\left(u(\xi)\right) = v\left(u(\xi), h_-\right), \qquad \text{for } \xi > \xi_1,$$

in view of (3.3). If $u_2 \in \left(u^A(h_-), u_+ = u^A(h_+)\right)$, then the failure of $(4.16)_2$ at $u = u_2$, still leads to $u'(\xi_2) \le 0$, a contradiction. These contradictions show that $(4.16)_2$ must be true if (4.3) has a solution.

The arguments in last paragraph already showed that the structure of $(u, h)(\xi)$ must as described by (4.17). At last, the uniqueness of the solution, up to a shift, follows directly from (4.17) and the uniqueness of solutions to initial-value problems for a system of ordinary differential equations. □

Remark 4.3. Theorem 4.3 establishes the existence of acceleration shocks. Notice that LWR model does not allow acceleration shocks. Acceleration shocks are not mentioned in existing literature as far as we know. However, many observations of real traffic, see e.g. Fig. 3 in Ref. 21 and Fig. 3 in Ref. 27, show that the acceleration front of a stop-and-go pattern can be as sharp as the deceleration shock serving as the other front, and the acceleration front is not visually expanding like a rarefaction wave. Thus, we think this sharp acceleration front is an acceleration shock.

The conditions of Theorem 4.3 cannot hold when $u_\pm > u_c$ because in that case $v = v^A(u)$ is the upper boundary there and it is concave.

Theorem 4.4. *Assume* $(u_\pm, h_\pm) \in \Omega$ *and* $h_- > h_+$. *The necessary and sufficient condition for* (4.3) *to have a solution is*

$$\begin{cases} u_- > u_+ = u^D(h_+), \quad \textit{and} \\ \dfrac{v_+ - v_-}{u_+ - u_-} > \dfrac{v(u,h_-) - v_-}{u - u_-} \quad \textit{for } u_- > u > u_+. \end{cases} \tag{4.21}$$

The solution is unique, up to a shift in ξ, *and its structure is*

$$u'(\xi) < 0 \quad \textit{and} \quad h(\xi) = \begin{cases} h_- & \textit{if } \xi < \xi_1, \\ h^D(u(\xi)) & \textit{if } \xi \geq \xi_1, \end{cases} \tag{4.22}$$

for some $\xi_1 \in \mathbb{R}$ *such that* $u(\xi_1) = u^D(h_-)$.

The proof is similar to that of Theorem 4.3 and hence is omitted.

In the rest of this section, we discuss the remaining basic waves of (3.2) which correspond to the usual Lax gas-dynamic waves. To simplify the presentation, we make the following further assumption:

Assumption (H): Assume (3.7), and

$$v^A_{uu}(u) < 0, \quad v^D_{uu}(u) < 0 \quad \text{and} \quad v^S_{uu}(u,h) < 0 \quad \text{for } (u,h) \in \Omega. \tag{4.23}$$

The second part of assumption (H) states the *concavity* of the functions v^A and v^D, as in Refs. 34, 43; the same requirement for v^S is made by analogy. This assumption is made for simplicity and according to the modeling in the existing literature. However, we stress that what follows *does not essentially depend* on this assumption: the possible concavity of one curve and convexity of the other, or even the existence of inflection points, only adds some technical difficulties but does not change the overall framework.

A rarefaction wave, see Ref. 10, of (3.2) is a solution of the form $(u,h)(\zeta)$, where $\zeta = x/t$. It satisfies equations

$$\begin{cases} -\zeta u' - (v(u,h))' = 0, \\ -\zeta h' = -\zeta \chi_A \left(h^A(u)\right)' - \zeta \chi_D \left(h^D(u)\right)', \\ (u,h)(\pm\infty) = (u_\pm, h_\pm). \end{cases} \tag{4.24}$$

Notice that because rarefaction waves are continuous, there is no need to consider a rarefaction wave that has parts in different modes since it, if exists, can be considered as a combination of multiple single-mode rarefaction waves. Thus, we only consider rarefaction waves in one mode only.

4.3. *Acceleration and deceleration waves*

The next lemma shows that the only waves connecting two points $(u_\pm, v_\pm)$ on the acceleration curve are rarefaction waves; they are called *acceleration rarefaction waves.*

Lemma 4.2. *Assume $u_\pm = u^A(h_\pm)$ and Assumption (H). If $u_- < u_+$, then there is a rarefaction curve connecting (u_-, h_-) with (u_+, h_+). If $u_- > u_+$, then neither shock nor rarefaction wave connections are possible.*

Proof. Assume $u_- < u_+$. Let $h = h^A(u)$. Since $v = v^A(u)$, then $(4.24)_1$ becomes

$$-\zeta = v_u^A\left(u(\zeta)\right), \tag{4.25}$$

when $u'(\zeta) \neq 0$. By (H) we have $v_{uu}^A < 0$, and then the function v_u^A can be inverted. We define

$$u(\zeta) = \begin{cases} u_- & \text{if } \zeta \leq -v_u^A(u_-), \\ (v_u^A)^{-1}(-\zeta) & \text{if } -v_u^A(u_-) < \zeta < -v_u^A(u_+), \\ u_+ & \text{if } \zeta \geq -v_u^A(u_+), \end{cases} \tag{4.26}$$

and $h(\zeta) := h^A\left(u(\zeta)\right)$. Then $(u,h)(\zeta)$ satisfies $(4.24)_{1,3}$. To show that it also satisfies $(4.24)_2$, we notice that from (4.25) it follows that $\zeta < 0$ and

$$-1 = v_{uu}^A u', \tag{4.27}$$

which implies $u' > 0$. Hence, we deduce $u_t = -\zeta u'/t > 0$ and so $(x,t) \in A$ by (4.5). Thus, Eq. $(4.24)_2$ is also satisfied since $h = h^A(u)$.

Now we prove that there is no rarefaction wave when $u_- > u_+$. When $u'(\zeta) \neq 0$, the equation $(4.24)_1$ yields

$$-\zeta = \chi_A v_u^A + \chi_D v_u^D + \chi_S v_u^S.$$

Then assumption (3.7) implies $\zeta < 0$ and (4.23) implies that u increases as $\zeta < 0$ increases. However, this contradicts the requirement $u(-\infty) = u_- > u_+ = u(\infty)$.

In the case of a shock wave, we have to prove that (4.3) has no solution when we assume $u_- > u_+$ and $u_\pm = u^A(h_\pm)$. Because of the condition $v_\pm = v^A(u_\pm)$, the jump condition (4.4) and $(3.7)_1$ imply $s < 0$. Hence by Lemma 4.1, both $u'(\xi)$ and $h(\xi)$ are continuous. By $(3.7)_1$, we also have

$$h_- = h^A(u_-) > h^A(u_+) = h_+. \tag{4.28}$$

For a solution $(u,h)(\xi)$ of (4.3), if it exists, to satisfy (4.28), it is necessary that for any subinterval $(h_1, h_2) \subset (h_+, h_-)$, there is $\xi_0 \in \mathbb{R}$ such that

$$h(\xi_0) \in (h_1, h_2) \quad \text{and} \quad h'(\xi_0) < 0.$$

This, combined with $(4.3)_2$, which states that

$$0 > h'(\xi_0) = u'(\xi_0)\left[\chi_A h_u^A + \chi_D h_u^D)\right]\big|_{\xi=\xi_0},$$

yields that $u'(\xi_0) < 0$ by $(3.7)_4$ and that either $\xi_0 \in A$ or $\xi_0 \in D$. By (4.6) it follows $\xi_0 \in D$, which implies $u(\xi_0) = u^D\left(h(\xi_0)\right)$. By the arbitrariness of (h_1, h_2), the value $h(\xi_0)$ can be chosen to be so close to h_+ that $u(\xi_0) = u^D\left(h(\xi_0)\right) \approx u^D(h_+) < u^A(h_+) = u_+ < u_-$. This infers that $u(\xi)$ is not monotone, violating Lemma 4.1. This completely proves the theorem. □

Analogously, the only waves connecting $(u_\pm, h_\pm)$ on the deceleration curve are shock waves; they are called *deceleration shock waves*. This is the content of the following lemma, whose proof is analogous to that of Lemma 4.2.

Lemma 4.3. *Assume $u_\pm = u^D(h_\pm)$ and Assumption (H). If $u_- > u_+$, then there is a shock curve connecting (u_-, h_-) with (u_+, h_+). If $u_- < u_+$ then no connection is possible.*

4.4. *Scanning waves*

If $(u_\pm, h_\pm)$ are on the same scanning curve then $h_- = h_+$. Eq. $(3.2)_1$ becomes $u_t - v(u, h_-)_x = 0$ while $(3.2)_2$ is trivially satisfied. Then system (3.2) reduces to a scalar conservation law. Thus, any two points $(u_\pm, h_- = h_+)$ on a scanning curve can be connected by a shock if $u_- > u_+$. When $u_- < u_+$, any two points $(u_\pm, h_- = h_+)$ can be connected by a rarefaction wave due to the $v^S_{uu} < 0$ in Assumption (H). We collectively call these waves as *scanning waves*.

Remark 4.4. At any fixed x and initial data $(u, h)(x, 0) \in \Omega$, if $h(\cdot, t)$ changes continuously as t increases, then $(3.2)_2$ enforces that

$$h = h^A(u) \text{ in } A \quad \text{and} \quad h = h^D(u) \text{ in } D. \tag{4.29}$$

The structure of shock waves given in (4.17) and (4.22) shows that (4.29) is still true inside the fine structure of a shock wave and that the transition from the S-mode to the A or D-mode inside the shock profile with $s < 0$ is continuous. This will make numerical computations a lot easier by making the discretization of $(3.2)_2$ unnecessary. Otherwise, the classical difficulty of handling the product of a jump discontinuity and a delta function, as well as the sensitivity of nonconservative quasilinear hyperbolic partial differential equations to the form of (numerical) viscosity would make the discretization of $(3.2)_2$ a difficult issue.

Remark 4.5. As in Remark 4.3, when $u_\pm > u_c$, the only available shocks involving different h's are either stationary shocks or and deceleration shocks along the deceleration curve. This is due to the fact in that case $v = v^A(u)$ is above $v = v^D(u)$ and then both chord conditions (4.16) and (4.21) fail when $u_\pm > u_c$ and $h_- \neq h_+$, unless both $(u_\pm, h_\pm)$ are on $v = v^D(u)$. By Theorem 4.3 and Theorem 4.4, the scanning to acceleration shocks and scanning to deceleration shocks do not exist when $u_\pm > u_c$.

5. An upwinding numerical method for (3.2)

Since eigenvalues for the hyperbolic system (3.2) are either negative or 0, we can use upwinding schemes for finding numerical solutions. Since the system (3.2) involves characteristic functions that depend on $\text{sign}(u_t)$, common upwinding schemes have to be modified to deal with them. To get started, we present a first order upwinding method for (3.2) on $\mathbb{R}$ in this section.

As usual, the numerical approximation of $f(x_j, t_n)$ is denoted as f_j^n, where $(x_j = j\Delta x, t_n = n\Delta t)$ are grid points for finite difference schemes. Given initial data $(u, h)(x, 0)$, the values (u_j^0, h_j^0) can be generated and $v_j^0 = v(u_j^0, h_j^0)$ can be computed. Note that if $(u, v) \in \Omega$ is given instead, then h can be computed by inverting $v = v(u, h)$ under Assumption (I′). To get (u, h) for later time steps, the following upwinding iteration formulas can be used:

$$\begin{cases} v_j^n = v(u_j^n, h_j^n), \\ u_j^{n+1} = u_j^n + \frac{\Delta t}{\Delta x}(v_{j+1}^n - v_j^n), \quad \text{first order upwinding scheme for } (3.2)_1, \\ \chi_A(x_j, t_n) = 1 \quad \text{if and only if } u_j^{n+1} > u_j^n \text{ and } u_j^{n+1} \geq u^A(h_j^n), \\ \chi_D(x_j, t_n) = 1 \quad \text{if and only if } u_j^{n+1} < u_j^n \text{ and } u_j^{n+1} \leq u^D(h_j^n), \\ \chi_S(x_j, t_n) = 1 \quad \text{if and only if } \chi_A(x_j, t_n) = 0 \text{ and } \chi_D(x_j, t_n) = 0, \\ h_j^{n+1} = \chi_A(x_j, t_n)h^A(u_j^{n+1}) + \chi_D(x_j, t_n)h^D(u_j^{n+1}) + \chi_S(x_j, t_n)h_j^n, \quad \text{compute } h_j^{n+1}. \end{cases} \tag{5.1}$$

The last equation in (5.1) is not a direct discretization of $(3.2)_2$; rather, it comes from the observation, made in Remark 4.4, that $(3.2)_2$ enforces $h = h^A(u)$ in A and $h = h^D(u)$ in D, and that the transition from S-mode to A or D-mode is continuous inside a shock profile when $s \neq 0$.

In a recent paper, see Ref. 13, the authors prove that the scheme (5.1) is total variation diminishing in v and h. If $v_u(u, h) > 0$, then the total variation of u is bounded. This guarantees that there is a convergent subsequence of (u_j^n, v_j^n, h_j^n).

All shock profiles in Section 4 are numerically verified by this scheme. The functions used in the numerical computation are $v^A(u) = 1-u^{-3}$, $v^D(u) = 1-u^{-1}/4$ and $u^D(h) = h$. We have $h_{\min} = 1/4$, and hence $u_0^A = 1.028$ is coordinate of the point of intersection of curves $h = 1/4$ and $v = v^A(u)$.

These simple functions satisfy the condition $v^D(1) = 0$ only up to a shift. This was only due to spare space in the following numerical figures but do not change the overall picture. To have some flexibility about scanning curves we use two positive parameters α and β as follows. We define $(u_1, v_1) := (u^D(h), v^D(u^D(h)))$; then we choose $u^A(h)$ as the solution of

$$v^A(u) = v_1 + \alpha(u - u_1),$$

from which its inverse $h = h^A(u)$ can also computed. The scanning curve $v^S(u, h)$ is a parabola passing through (u_1, v_1) and $(u_2, v_2) := \left(u^A(h), v^A(u^A(h))\right)$,

$$v^S(u, h) = v_1 + N_1(u - u_1) + N_2(u - u_1)(u - u_2)$$

where $N_1 := (v_2 - v_1)/(u_2 - u_1)$ and $N_2 := -N_1/[\beta(u_2 - u_1)]$. The parameters α and β are chosen to satisfy Assumption (I′) at least in the range of (u, h) for the computation. In all plots of numerical solutions shown in this paper, the parameters are $\alpha = 0.1, \beta = 1.1$, $\Delta x = 1/1000$th of the range of x shown in plots, and $\Delta t = 0.2\,\Delta x$.

6. Solutions of Riemann problems

In this section we find solutions of system (3.2) for Riemann initial data

$$(u,h)(x,0)=\begin{cases}(u_-,h_-) & \text{if } x<0,\\ (u_+,h_+) & \text{if } x>0,\end{cases} \tag{6.1}$$

under the further Assumption (H). These solutions are of the form $(u,h)(\xi)$ where $\xi=x/t$. We call such solutions Riemann solutions. We use for brevity the following notations: S denotes shock waves, R rarefaction waves, ST stationary waves, ScS scanning shock and ScR scanning rarefaction waves, AR acceleration rarefaction waves, DS deceleration shocks, ScDS scanning-to-deceleration and ScAS scanning-to-acceleration shocks. We denote $v_\pm=v(u_\pm,h_\pm)$ and describe solutions in the (u,v)-plane, instead of using the (u,h)-plane of the states, because this is more intuitive, and by assumption (H) the two approaches are clearly equivalent.

To simplify the description of solutions' wave structure, we make the assumption (H) stricter by assuming that $v^S_{uu}<0$.

6.1. *Case 1.* $u_-\geq u_c$

In this case, Riemann solutions are of the following forms; we refer to Fig. 6.

(i) If $v^A\left(u^A(h_-)\right)\geq v_+\geq v_-$, then a Riemann solution is of the form

$$(u_-,v_-)\xrightarrow{\text{ScR}}(u_m,v_+)\xrightarrow{\text{ST}}(u_+,v_+), \tag{6.2}$$

which is a short way to express the solution

$$(u,v)(\xi)=\begin{cases}(u_-,v_-) & \text{if } \xi<-v^S_u(u_-,h_-),\\ \left((v^S_u)^{-1}(-\xi,h_-),v(u(\xi),h_-)\right) & \text{if } -v^S_u(u_-,h_-)\leq\xi\leq-v^S_u(u_m,h_-),\\ (u_m,v_+) & \text{if } -v^S_u(u_m,h_-)<\xi\leq 0,\\ (u_+,v_+) & \text{if } \xi>0,\end{cases}$$

where u_m satisfies $v^S(u_m,h_-)=v_+$. The part in the solution that corresponds to the rarefaction wave $(u_-,v_-)\xrightarrow{\text{ScR}}(u_m,v_+)$ is provided by the second line above. It is obtained from the rarefaction wave equation (4.24) along the scanning curve $h=h_-$, which yields $-\xi=v^S_u(u,h_-)$ and hence $u(\xi)=(v^S_u)^{-1}(-\xi,h_-)$. The speeds of waves in (6.2) are required to be in ascending order from the left to right, which they are, so that the solution's detailed form is well defined. Speeds of rarefaction waves are read from the fundamental diagram in (u,v)-plane as $-v_u$, while that for shocks they are read from the slope of the line connecting $(u_\pm,v_\pm)$ in the (u,v)-plane, as given by (4.4).

(ii) If $v_+>v^A\left(u^A(h_-)\right)\geq v_-$, then

$$(u_-,v_-)\xrightarrow{\text{ScR}}\left(u^A(h_-),v^A(u^A(h_-))\right)\xrightarrow{\text{AR}}\left(u_m,v_+=v^A(u_m)\right)\xrightarrow{\text{ST}}(u_+,v_+).$$

For simplicity, the detailed forms of Riemann solutions are omitted from now on.

(iii) If $v_+ < v_-$, then

(a) either

$$(u_-, v_-) \xrightarrow{\text{ScS}} \big(u^D(h_-), v^D(u^D(h_-))\big) \xrightarrow{\text{DS}} \big(u_m, v_+ = v^D(u_m)\big) \xrightarrow{\text{ST}} (u_+, v_+),$$

if there exists $\big(u_m, v_+ = v^D(u_m)\big)$ such that the speed of the deceleration shock DS is less then that of the scanning wave. Since all velocities are negative, the lesser the velocity the steeper is the chord joining the states.

(b) or, if the previous condition is not met, then

$$(u_-, v_-) \xrightarrow{\text{ScDS}} \big(u_m, v_+ = v^D(u_m)\big) \xrightarrow{\text{ST}} (u_+, v_+).$$

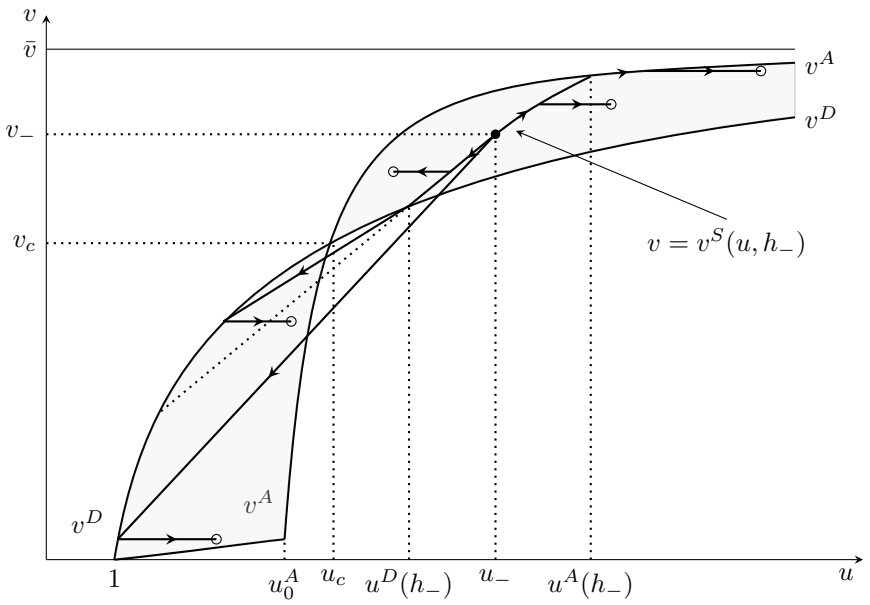

Fig. 6. Riemann solutions in Case 1. The state (u_-, v_-) is represented by a full circle; various states (u_+, v_+) are represented by empty circles. The oblique dotted line, whose slope is $v_u^S\big(u^D(h_-), h_-\big)$, separates case *(ii)(a)*, which occurs above that line, from case *(ii)(b)*, which occurs below.

6.2. *Case 2.* $u_- < u_c$

As in the previous case, solutions are classified depending on v_+. We refer to Fig. 7.

(i) If $v_+ \le v^D(h_-)$, then

$$(u_-, v_-) \xrightarrow{\text{ScDS}} \big(u_m, v_+ = v^D(u_m)\big) \xrightarrow{\text{ST}} (u_+, v_+).$$

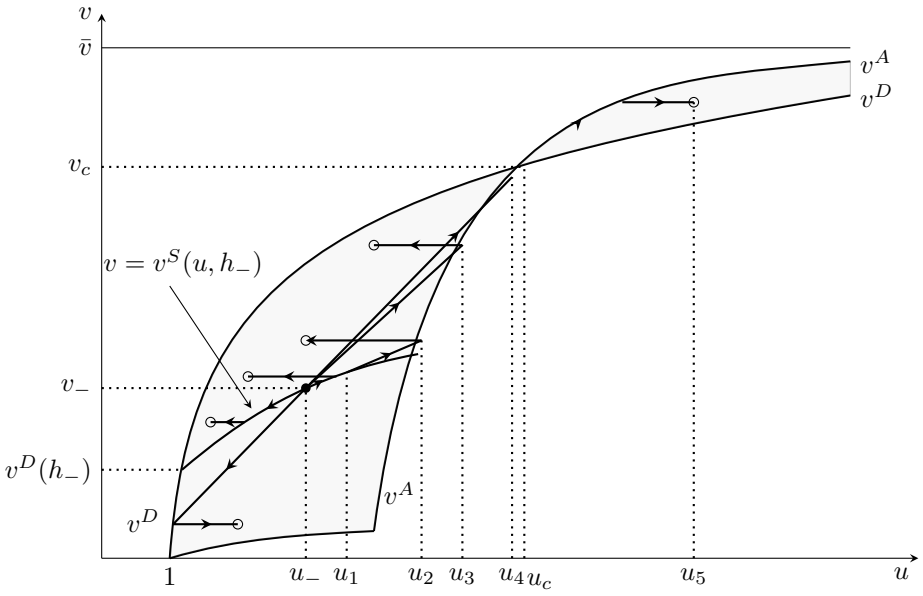

Fig. 7. Riemann solutions in Case 2. Notations are as in Fig. 6.

(ii) If $v^D(h_-) \le v_+ \le v_-$, then

$$(u_-, v_-) \xrightarrow{\text{ScS}} \big(u_m, v_+ = v^S(u_m, h_-)\big) \xrightarrow{\text{ST}} (u_+, v_+).$$

(iii) If $v_+ > v_-$, then the solution is one of the following, in order of increasing v_+:

(a) either

$$(u_-, v_-) \xrightarrow{\text{ScR}} \big(u_m, v_+ = v^S(u_m, h_-)\big) \xrightarrow{\text{ST}} (u_+, v_+);$$

(b) or

$$(u_-, v_-) \xrightarrow{\text{ScR}} \big(u_1, v_1 = v^S(u_1, h_-)\big) \xrightarrow{\text{ScAS}} \big(u_2, v^A(u_2) = v_+\big) \xrightarrow{\text{ST}} (u_+, v_+),$$

where the chord connecting (u_1, v_1) and (u_2, v_2) is tangent to the curve $v = v^S(u, h_-)$ at $u = u_1$;

(c) or

$$(u_-, v_-) \xrightarrow{\text{ScAS}} \big(u_3, v^A(u_3) = v_+\big) \xrightarrow{\text{ST}} (u_+, v_+);$$

(d) or, at last,

$$(u_-, v_-) \xrightarrow{\text{ScAS}} \big(u_4, v^A(u_4)\big) \xrightarrow{\text{AR}} \big(u_5, v_+ = v^A(u_5)\big) \xrightarrow{\text{ST}} (u_+, v_+),$$

where the chord connecting (u_-, v_-) and $\big(u_4, v^A(u_4)\big)$ is tangent to the curve $v = v^A(u)$ at $u = u_4$.

Example 6.1 (Car train with stationary but varying spacing). A car train is defined as a platoon of cars traveling at the same constant speed $v(x,t) \equiv v_0$, but the spacing $u(x,t) = u_0(x)$ does not have to be uniform in x. This is the result of different driving tastes (or hysteresis moods) for spacing. It is easy to see that $(u,v)(x,t) = (u_0(x), v_0)$ is a solution of (3.2), as long as $(u_0(x), v_0) \in \Omega$ for all $x \in \mathbb{R}$.

It is not a surprise that stationary shocks appear so often in Riemann solutions, since 0 is an eigenvalue of system (3.2), see (3.8); the waves associated to this linearly degenerate eigenvalue are contact discontinuities.

Are there other Riemann solutions for the same initial data? Indeed, for many initial data (6.1), there are infinitely many Riemann solutions, and some of them do not use stationary shocks. However, we claim that other solutions are a waste of drivers' effort and fuel without much to gain for both the driver initiating those Riemann solutions and those drivers behind. To see this, consider the initial data (6.1) with $(u_\pm, v_\pm)$ as in Fig. 8. Because $v_- > v_+$, the driver of the first car at the

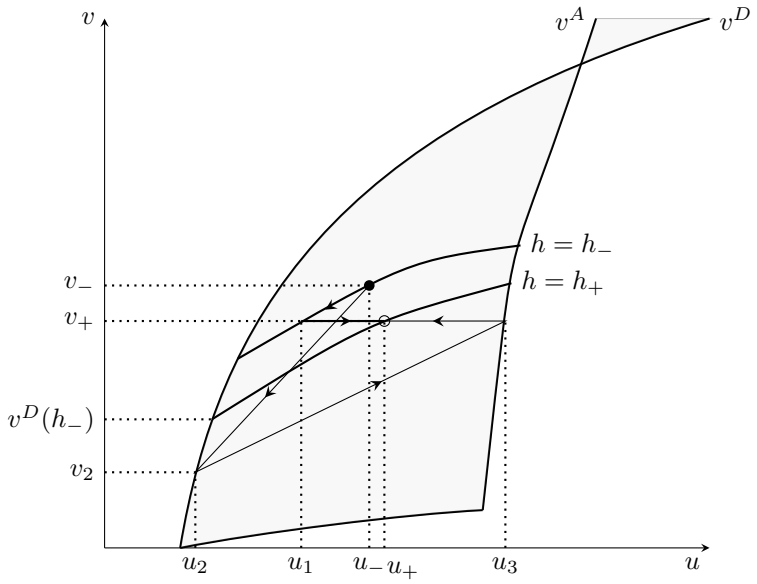

Fig. 8. Two different solutions for the same initial data. The solution proposed in Case 2*(ii)* is depicted with thick lines, the other one with thin lines.

$\{x < 0\}$ part will have to decelerate. The Riemann solution listed in Case 2*(ii)* for this initial data is

$$(u_-, v_-) \xrightarrow{\text{ScS}} (u_1, v_+) \xrightarrow{\text{ST}} (u_+, v_+), \tag{6.3}$$

which says that the driver first slows down to state (u_1, v_+) on the scanning curve

$h = h_-$ to speed v_+, the same as the car in front. *Once the speed is slowed down to the speed v_+ of the platoon in front of the driver, there is no incentive for him/her to slow down more*, and hence he/she will keep the speed v_+ afterwards, resulting in the stationary shock at $x = 0$. In this sense, all Riemann solutions listed in Cases 1 and 2 are "rational" Riemann solutions. This rational driver's behavior is the reason for stationary shocks appearing in Riemann solutions.

Whether the "rational" Riemann solution is unique is left for future investigations.

However, as long as the scanning curves' slopes are relatively small, there are also infinitely many other Riemann solutions of the form

$$(u_-, v_-) \xrightarrow{\text{ScDS}} (u_2, v_2) \xrightarrow{\text{ScR or ScAS}} (u_3, v_+) \xrightarrow{\text{ST}} (u_+, v_+), \tag{6.4}$$

as illustrated in Fig. 8 for the case when the second wave is a scanning-to-acceleration shock. This solution form corresponds to the situation where the driver of the first car at $x = 0-$ overdecelerates to speed $v_2 < v_+$, possibly due to applying brake late or to other random reasons, forcing cars behind him also to decelerate to the velocity v_2 and with a denser spacing u_2. Because $v_2 < v_+$, the spacing in front of the first car at $x = 0-$ improves as t increases. This induces the driver to speed up to v_+, either through a scanning rarefaction wave, or a scanning to acceleration shock, and then keep the speed v_+ with a more comfortable spacing u_3. Both solution types (6.3) and (6.4) are possible, depending on the driver's actions. Comparing with (6.3), solutions of shape (6.4) certainly require more driver's effort and more cost in fuel and car maintenance, without any saving in travel time. If the driver for the car at $x = 0-$ is rational, he/she should act according to (6.3). However, there is nothing stopping him/her to act as in (6.4), either by error or intention. Accommodating different drivers' choices, the model (3.2) has different Riemann solutions for them, as it should do.

Remark 6.1. The upwinding scheme presented in Section 5 are tested to compute numerical Riemann solutions; all of them agree with the "rational" Riemann solutions presented in this section.

7. Stop-and-go waves, existence and non-existence

In this section we show, by examples, solutions of initial value problems of the system (3.2) to see its capability of exhibiting several well-known traffic flow phenomena, emphasizing on those where LWR model fails. Solutions are constructed via front tracking using Riemann solutions constructed in Section 6, unless otherwise stated. To simplify notations, in the following we often identify states (u_1, v_1), (u_2, v_2) with circled numbers as ①, ② and so on.

Example 7.1 (Stop-and-go solutions in $u < u_c$ zone). Pick any two points ① $= (u_1, h_1)$ and ② $= (u_2, h_2)$ shown in Fig. 9 on the left, such that $u_1 = u^D(h_1)$, $u_2 = u^A(h_2)$, and both chord conditions (4.16) and (4.21) are assumed to hold. This can happen in the zone $u < u_c$.

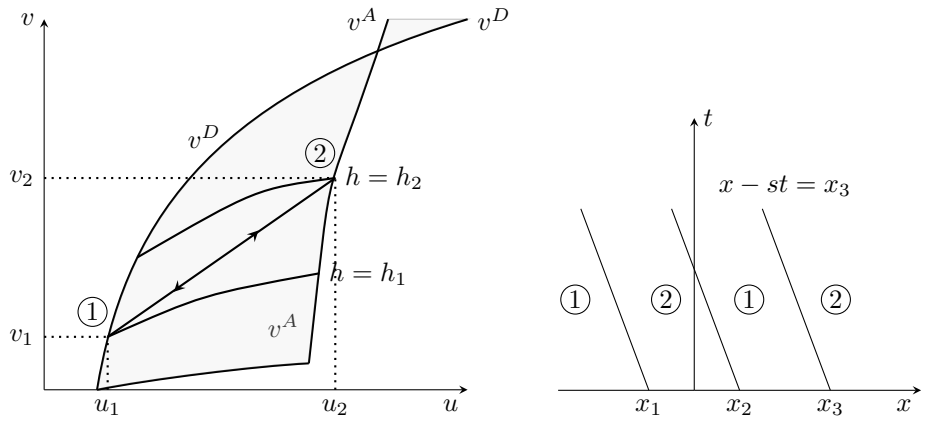

Fig. 9. Stop-and-go solutions: left, in the (u, v)-plane; right, in the (x, t)-plane.

By Theorem 4.3 there is a shock wave from (u_1, v_1) to (u_2, v_2) and, by Theorem 4.4, there is another shock wave from (u_2, v_2) to (u_1, v_1); both shock waves have the same speed $s < 0$. Stop-and-go solutions can be constructed using these two shocks. For example, consider the solution (u, v) of the inviscid system (3.2), shown in Fig. 9 on the right. The speeds of cars at any given time t alternate as x increases, from slow (with velocity v_1) to fast (with velocity v_2). Furthermore, the wave pattern shape is steady because all boundaries of speed alternation travel at the same speed $s < 0$, so that the length of each speed zone does not change.

To see how a hysteresis loop enables a stop-and-go wave, look at the fine structure of the viscous shocks ① → ② and ② → ① that form a stop-and-go wave. To connect (u_1, h_1) to (u_2, h_2) (or vice versa), the viscous profile $(u, h)(\xi)$ first moves along the scanning curve $h = h_1$ (or $h = h_2$) as ξ increases from $-\infty$ to reach the state $(u, h) = (u^A(h_1), h_1)$ (or $(u, h) = (u^D(h_2), h_2)$) on the acceleration (or deceleration) curve. Then it moves along the acceleration (or deceleration) curve to arrive to the final state (u_2, h_2) (or (u_1, h_1)). In other words, the fine structure of the profile of one front of a stop-and-go wave covers a half of a hysteresis loop. Another front of the stop-and-go covers the other half of the loop to complete a *whole hysteresis loop* by returning to the original state. It is the hysteresis loop in the direction required by chord conditions (4.16) and (4.21) that makes the coexistence of two shocks forming the two fronts of a stop-and-go wave possible. This explains the relation between stop-and-go waves and hysteresis loops.

In contrast, traffic models of form of hyperbolic conservation laws cannot produce such steady shaped stop-and-go solutions, because if one shock satisfies the Lax condition, the other will violate it.

When h_1 and h_2 are close, then the shock ① → ② has to be replaced with

$$① \xrightarrow{\text{ScR on } h = h_1} (u_m, v_m) \xrightarrow{\text{ScACD}} ②,$$

where (u_m, v_m) is the point on the scanning curve $h = h_1$ that can connect to ② with a scanning-to-acceleration-shock which is a contact discontinuity. The shape is not steady as these waves travels at different speeds and hence will interact later. The interaction can take a long time to finish if the curves of the fundamental diagram are close to being straight. In this sense, the solution can still be considered as a stop-and-go wave for practical purposes.

In Ref. 44, the authors observed empirically stop-and-go waves in actual traffic, and found that the speed in congestion (v_1) and that at the outflow of congestion (v_2) can range broadly, from 6.3 to 48.7 km/h for v_1 and from 29.3 to 61.2 km/h for v_2. The solution construction shown above indeed allows wider range of choices for v_1 and v_2 as long as they differ sufficiently in the zone $u < u_c$.

The previous construction of stop-and-go solutions is not possible if one or both u_1 and u_2 are in the range $u > u_c$. To see this, assume $h_1 < h_2$ without loss of generality. The existence of the shock ① → ② requires the chord condition (4.16), which can be satisfied only if $v = v(u, h_1)$ is below the chord for u between u_1 and u_2, while that for the shock ② → ① requires $v = v(u, h_2)$ to be above the chord. They cannot both be satisfied if $v^A(u)$ is above $v^D(u)$, which is what happens in the range $u > u_c$. Thus, *the model* (3.2) *predicts that there is no steady shaped stop-and-go wave in the zone where* $v^A(u)$ *is above* $v^D(u)$*, which happens when* $u > u_c$.

Example 7.2 (Formation of stop-and-go waves in $u < u_c$). We show that, in an otherwise uniform car platoon, sufficient deviation from the uniform speed by few cars can generate a stop-and-go wave. Consider a car platoon with constant spacing and speed $(\bar{u}, \bar{v})$ (a car train for short) with $\bar{u} < u_c$. Assume $(\bar{u}, \bar{v})$ is in the interior of Ω, as shown in Fig. 10 on the left. What is the effect if cars in the range $-1 < x < 0$ brake to a lower speed $v_1 < \bar{v}$, due to a temporary bottleneck at $x = 0$?

To simulate this situation, consider the initial data

$$(u,v)(x,0) = \begin{cases} (u_1, v_1) =: ① =: C1 & \text{if } x < -1, \\ (u_2 = u_1, v_2) =: ② =: C2 & \text{if } -1 \le x \le 0, \\ (u_1, v_1) = ① & \text{if } x > 0, \end{cases} \tag{7.1}$$

where $u_1 = u_2$ and both (u_1, v_1) and (u_2, v_2) are in the interior of Ω. All the shock connections in Fig. 10 exist if both scanning curves $h = h_1$ and $h = h_2$ are sufficiently flat or v_2 is low enough with respect to v_1. We refer to Fig. 11 for numerical simulations using the upwinding scheme proposed in Section 5. In those figures, the phase state $(u, v) = ⓝ$ is denoted by Cn.

The initial jumps at $x = -1$ and $x = 0$ are solved (see cases 2*(ii)* and 2*(iii)(c)* in Section 6) respectively as

$$① \xrightarrow{\text{ScDS}} ③ \xrightarrow{\text{ST}} ②, \qquad ② \xrightarrow{\text{ScAS}} ④ \xrightarrow{\text{ST}} ①.$$

At time $t = t_1$, the stationary shock ③ $\xrightarrow{\text{ST}}$ ② meets the scanning-to-acceleration

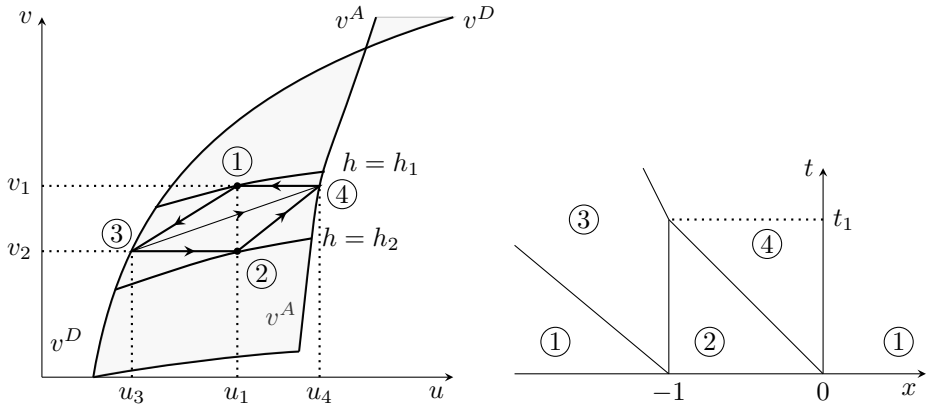

Fig. 10. Formation of a stop-and-go pattern. On the left, thick lines are waves produced at $t = 0$ and thin lines are the shock waves emitted at $t = t_1$. On the right, the solution in the (x, t)-plane.

shock ② $\xrightarrow{\text{ScAS}}$ ④ at $x = -1$. This interaction is solved by just one scanning-to-acceleration shock ③ $\xrightarrow{\text{ScAS}}$ ④, see Fig. 10 on the right. This scanning-to-acceleration shock's speed is slower than that of ① $\xrightarrow{\text{ScDS}}$ ③, and hence there is no wave interaction after $t = t_1$. The stop-and-go speed oscillation $\bar{v} \to v_1 \to \bar{v}$ is then generated and will persist as t increases. Thus, the model (3.2) shows that phantom jam can be created in a uniform car train in congested zone by a few cars' random braking that create large enough speed variation. Notice that the numerical solution is in perfect agreement with the analysis presented in Fig. 10.

If v_2 is sufficiently larger than v_1 in $\{u < u_c\}$ zone, similar wave patterns emerge.

Example 7.3 (Formation of stop-and-go waves on a closed circular track). Stop-and-go waves can emerge just by human drivers' behavior alone, without any influence by lane changing or by road features. This was experimentally shown by letting cars travel in a one-lane ring road, see Ref. 39, where initially uniform car platoons were observed to develop stop-and-go patterns later, and a jam region propagated upstream through otherwise faster moving cars. Model (3.2) can exhibit the formation of such patterns. To see this, we continue Example 7.2 by considering a circular road. Recall that the Lagrange coordinate x is a label of cars. The car platoon on a circular road must satisfy the periodic boundary condition

$$(u, v)(x + L, t) = (u, v)(x, t), \tag{7.2}$$

where $L > 2$ is the number of cars in the circular lane. The initial data (7.1) is modified as

$$(u, v)(x + nL, 0) = (u, v)(x, 0) = \begin{cases} (\bar{u}, \bar{v}) = ① & \text{if } -L/2 \le x < -1, \\ (\bar{u}, v_1) = ② & \text{if } -1 \le x \le 0, \\ (\bar{u}, \bar{v}) = ① & \text{if } 0 < x < L/2, \end{cases} \tag{7.3}$$

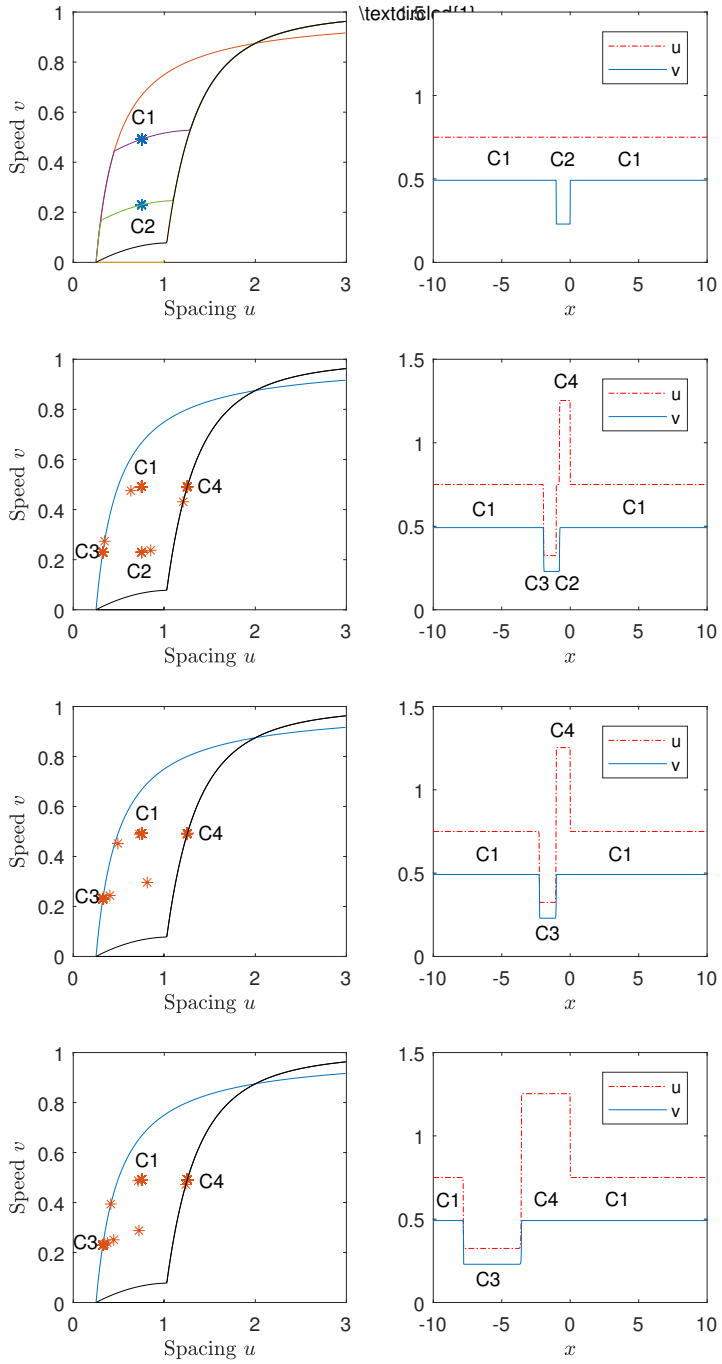

Fig. 11. The solution of Example 7.2. First line, $t = 0$: initial data in the (u, v) and (x, uv)-plane. Second line, $t = 1.5 < t_1$; on the right, there are four shocks, the second and the last from the left are stationary. Third line, $t = 2 > t_1$; the two shocks in the middle when $t < t_1$ merge into one shock. Fourth line, $t = 11 > t_1$; the slow region in the middle expands. Plots are as predicted in Fig. 10.

for $n = \pm 1, \pm 2, \ldots$.

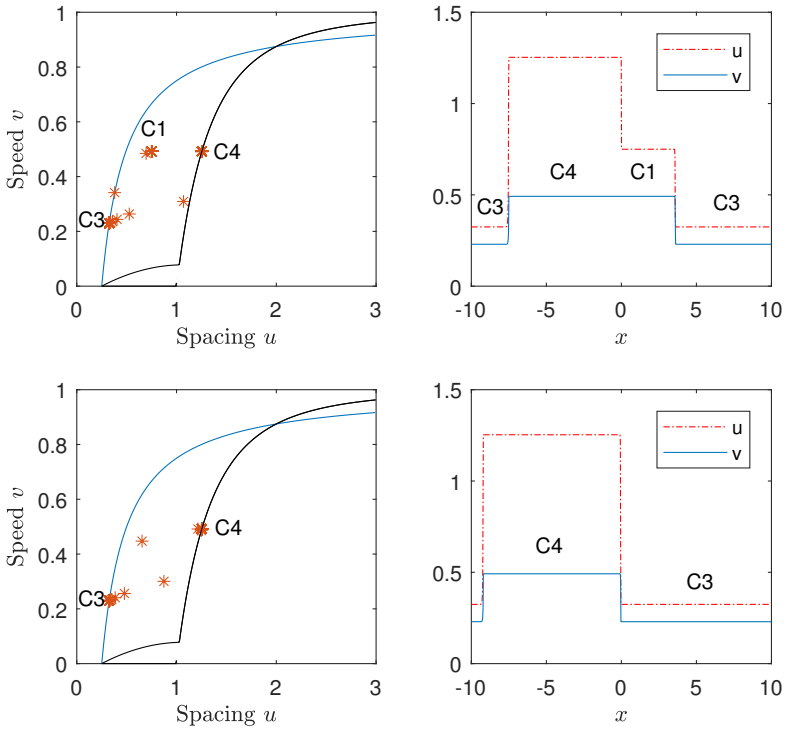

Fig. 12. The solution of Example 7.3. First line: $t = t_3 > t = 25 > t_2$; the leftmost shock in Fig. 11, fourth line, already moved across $x = -L/2$, which is equivalent to $x = L/2$, to the left and arrived at $x \approx 4$ at $t = 25$. This shock will continue to move to the left to interact with the stationary shock at $x = 0$. Second line: $t = 31$. The rightmost and the stationary shock at $x = 0$ in Fig. 12 combine into one scanning-to-deceleration shock. The stop-and-go wave appears. The pattern persists after $t = t_3$.

Fig. 10 on the right is still correct, if L is large enough, until the leftmost shock ① $\xrightarrow{\text{ScDS}}$ ③ hits $x = -L/2$, equivalent to $x = L/2$ on the circular lane, at time $t = t_2 > t_1$. After $t = t_2$, this shock continues to move to the left from $x = L/2$ to hit $x = 0$ at time $t = t_3$. Then, at $t = t_3+$, the cars on the circular track are divided into two segments separated by two shocks ③ $\to$ ④ and ④ $\to$ ③. One is the ③ $= (u_3, v_3 = v_2)$ region where the traffic is denser and slower, the other is the ④ $= (u_4, v_4 = v_1)$ zone in which the traffic is sparser and faster. Because the speed of the two shocks ③ $\to$ ④ and ④ $\to$ ③ is the same, this wave pattern is steady after t_3.

Numerical solution for this example can be obtained by continuing for $t > 11$ the numerical solution shown in Fig. 11, last line, from Example 7.2 under the periodic boundary condition. The result is shown in Fig. 12, illustrating the solution before

and after $t = t_3$. The numerical solution after $t = t_3$ has a steady shape stop-and-go pattern that travels upstream to the left.

If v_2 is moderately smaller than v_1, then at fixed time right after t_2+, the wave pattern in v is, from upstream down, a slowdown shock and a rarefaction speedup wave (followed by a contact-discontinuity acceleration-shock if $|v_1 - v_2|$ is larger). These regions travel upstream. As t further increases, more wave interactions will occur. Our numerical simulations show that the wave pattern for v is not steady, but can remain for a long time while the variation of v decays as the rarefaction wave and the leftmost deceleration shock interact.

From Fig. 10, it is clear that if the slope of the scanning curve is small, then it takes less deviation in speed, $\bar{v} - v_1$, to produce a stop-and-go pattern.

Example 7.4 (Speed disturbances by a few cars in an otherwise uniform car train in $u > u_c$ dissipates.). Example 7.2 shows that a large enough speed disturbance in an otherwise uniform car train traveling in congested zone $u < u_c$ can generate a persistent stop-and-go wave. It is natural to investigate the effect of a large enough temporary bottleneck on an otherwise uniform car train traveling in the free zone $u > u_c$. To mimic such situation, consider the initial data in Fig. 13, representing an otherwise uniform car train traveling with state ①, and a few cars that travels temporarily at a much slower state ②. The solution constructed in Fig. 13 on the right shows that, after some time, cars travels in either state ① or ③, all of them with the original fast speed v_1. The effect of these few slow cars at the initial time is eliminated in a finite time. Notice that the wave from ② to ③ is composed by a deceleration-to-acceleration shock glued on the left to an acceleration rarefaction wave.

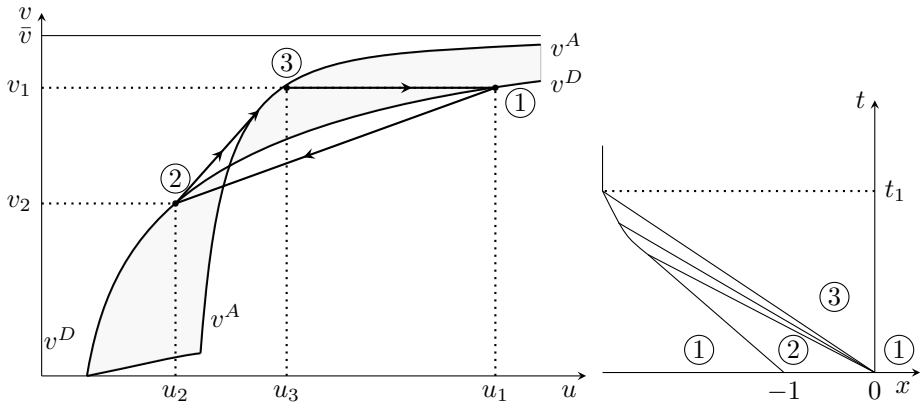

Fig. 13. Few temporarily slow cars in an otherwise uniform car train in the free zone have no effect on car platoon's speed after time t_1.

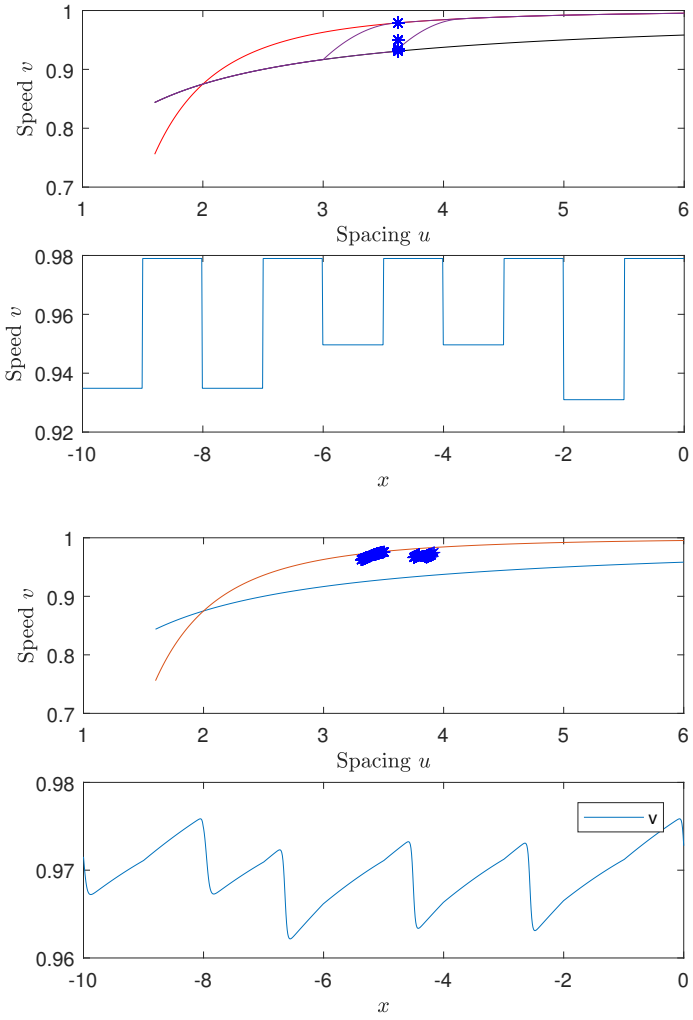

Fig. 14. The solution of Example 7.5. First and second lines, $t = 0$: initial data. The amplitude of speed oscillation is 0.048, out of the maximum speed 0.97. Third and fourth lines: $t = 50$. The amplitude of speed oscillation is 0.0138, only 30% of the initial amplitude.

Example 7.5 (Speed oscillations in $u > u_c$ zone dissipates.). We further illustrate that speed oscillations in a platoon dissipate when the acceleration curve is above the deceleration curve. To this aim, consider the initial data shown in Fig. 14 having speed oscillations in a car platoon. The boundary condition is periodic to simulate traffic on a ring road. We observe that the speed oscillations in the numerical solution are smoothed as time increases: Fig. 14, third and fourth lines, shows that at time $t = 50$ the amplitude of speed oscillations decays to less than

30% of that at $t = 0$.

Remark 7.1. The above examples show that the model (3.2) exhibits stop-and-go waves when the acceleration curve lies below the deceleration curve, i.e., in the $u < u_c$ zone. A sufficient deviation of speed by a few cars in a platoon in the $u < u_c$ zone creates stop-and-go waves in the platoon. On the other hand, when $v = v^A(u)$ is above $v = v^D(u)$, i.e. in the $u > u_c$ zone, the model predicts that there are no stop-and-go waves and the amplitude of speed oscillations dissipates as time passes. According to the terminology often used in traffic modeling, see Refs. 16, 22, 23, the region $\{u > u_c\}$ is the *free zone* and the region $\{u < u_c\}$ is the *congested zone*. The above examples confirm this terminology.

8. A possible mechanism of jam formation

We continue to investigate the formation, growth and decay of phantom jams.

Example 8.1 (Decay of a stop-and-go wave due to sparser vehicles upstream or downstream). Let us continue to consider Example 7.1 and Fig. 9. Intuitively, the deceleration wave will decay if the car platoon *upstream* is sparse enough, so that the upstream state is more "compressible" and can absorb the deceleration wave. To test whether the model (3.2) agrees with this observation, we set up the initial data as

$$(u,v)(x,0) = \begin{cases} (u_3,v_3) = ③ \ \text{ if } x \le -2, \\ (u_1,v_1) = ① \ \text{ if } -2 < x < -1, \\ (u_2,v_2) = ② \ \text{ if } -1 \le x \le 0, \\ (u_1,v_1) = ① \ \text{ if } x > 0, \end{cases} \tag{8.1}$$

where $u_3 >> u_2$. For convenience, select $v_3 = v^D(u_3)$, see Fig. 15. This simulates the situation where there is a stop-and-go wave moving upstream (modeled in the initial data through the sequence ①②①) and the traffic upstream is in free zone with spacing u_3 sparse enough. In such a case, the slope of the line connecting states ③ and ④ is small enough such that the shock connecting ① and ② will eventually interact; this eliminates the slow region with slow speed v_2 after time t_3. The solution of (3.2) in (x,t)-plane is depicted in Fig. 15 on the right.

Another way for the stop-and-go waves, as is for any traffic jam, to disappear in time is that the *downstream* traffic travels faster. To confirm that the model (3.2) exhibits this phenomenon, we set the initial data as is shown in Fig. 16 on the right. The downstream traffic is faster, with $v_3 > v_2$. Choose $v_3 = v^A(u_3)$ for simplicity. The solution depicted in Fig. 16 shows that, in a finite time, the slow region with speed v_2 is eliminated and every car's speed will eventually increase to v_3.

Example 8.2 (Decay of phantom jam caused by small disturbance). Example 7.2 shows that when a few cars in an otherwise uniform (in speed and spacing) platoon of cars deviate in speed by a sufficient margin, then stop-and-go patterns appear and persist as t increases. In this example, we investigate what happens

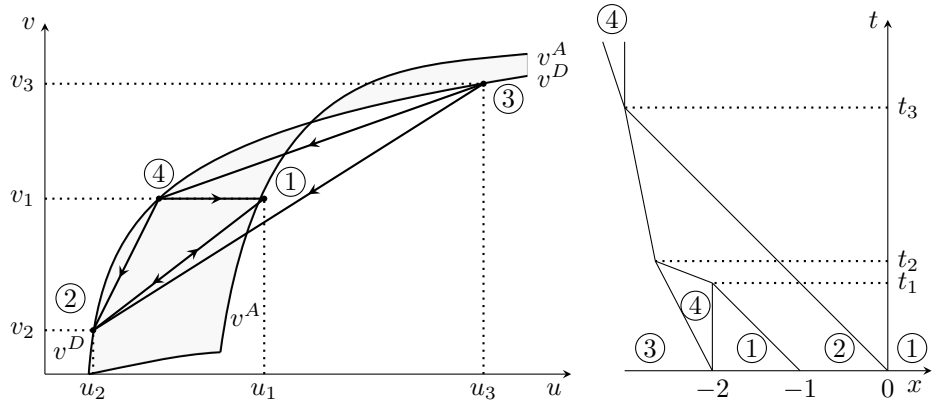

Fig. 15. Decay of a stop-and-go wave due to sparser vehicles upstream.

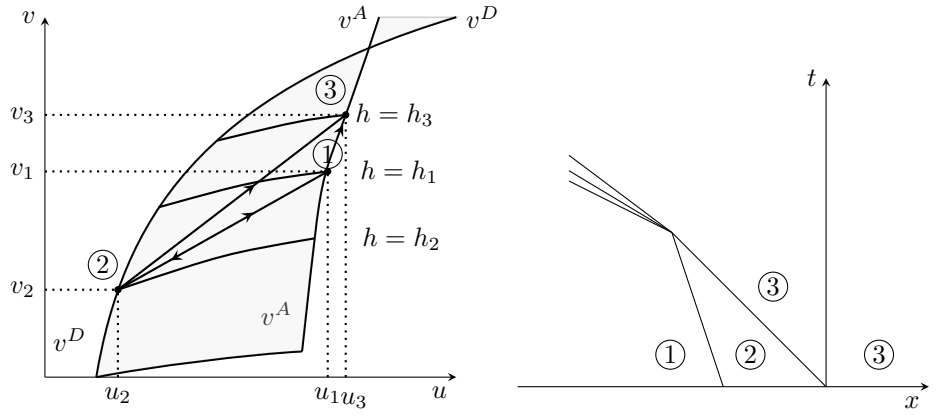

Fig. 16. The slow region in the middle of a stop-and-go wave disappears in time when the traffic downstream is faster.

when the deviation is small. Notice that, differently from Example 7.2, cars never reach the acceleration and deceleration curves; the small disturbance is simulated by imposing that the traffic flow is strictly contained in the scanning zone.

Assume $v_2 < v_1$ for definiteness; the arguments and results for the other case are similar. Consider the initial data given by (7.1) with v_2 close enough to v_1 so that ③ and ④ are inside Ω, see Fig. 17 on the left. This requires ① $= (u_1, v_1)$ and ② $= (u_2 = u_1, v_2)$ to be away from the curves $v = v^A(u)$ and $v = v^D(u)$.

The solution constructed using the Riemann solutions listed in Case 2 in Section 6 is illustrated in Fig. 17 on the right. The interaction of the scanning rarefaction wave ② $\xrightarrow{\text{ScR}}$ ④ and the stationary shock ③ $\xrightarrow{\text{ST}}$ ② shifts the rarefaction wave along the $h = h_2$ scanning curve to that of $h = h_1$. Later, this rarefaction wave

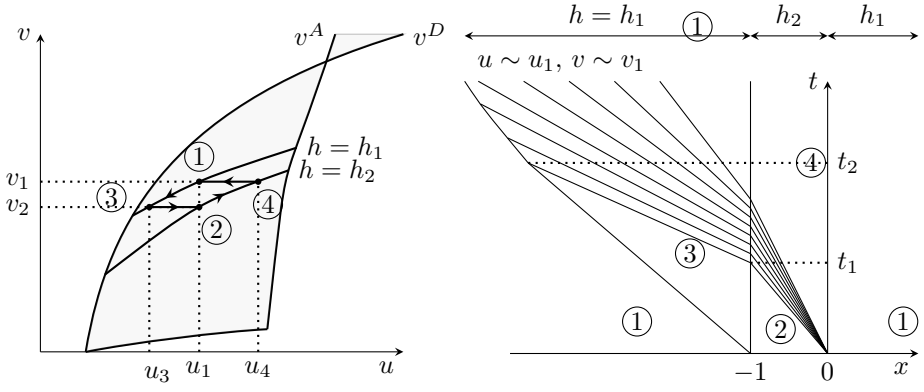

Fig. 17. The disturbance of speed by a few cars slightly slower in an otherwise uniform platoon of cars will decay, but the sparser region created in front of these few cars is persistent. Left: in the (u, v)-plane; right: in the (x, t)-plane.

with $h = h_1$ will interact with the scanning shock of the same h_1 and will eliminate the slow region with state ③. This interaction is due to the nonlinearity of the scanning curve. Further interaction of the rarefaction and the shock wave will make cars' states in the interaction zone go to ①.

It is interesting to see that the final state of the car train has spacing almost equal to u_1 except for cars in $-1 < x < 0$, where it is u_4 wider than u_1. This is intuitive in the sense that cars in $-1 < x < 0$, which are initially slower than cars in $x > 0$, will have more space in front because it takes time for them to accelerate to v_1, and stay at that speed afterwards. The cars initially behind $x = -1$ first have to slow down to speed v_2, and later accelerate back to v_1. Since they change speed along the same scanning curve, their spacing also return to the original u_1. This phenomenon is disallowed in LWR model because it specifies $v = v(u)$, making different spacing for the same speed impossible.

Similarly, if the few cars in the otherwise uniform car train in congested region are faster instead, then the disturbance in speed will also decay, but the spacing for those faster cars at $t = 0$ will be more compact while the spacing for other cars remains almost the same after some time.

Remark 8.1. The last examples suggest that if a few cars in an otherwise uniform car train brake sufficiently relative to slopes of the scanning curves nearby, then a stop-and-go phantom jam is created and the jam will persist. On the other hand, if the slowing down or speeding up is minor, then the speed oscillation in the car platoon will decay in time, if the initial data are strictly in scanning region. When the deviation from the uniform speed is up, then the can train will become denser for those cars overspeeding at $t = 0$. Else, the spacing for these cars become larger.

As a conclusion, if drivers are more likely to overspeed a little than underspeed in an otherwise uniform car train, then the car train will become more and more

compact, until the state (u, v) reaches the curve $v = v^D(u)$ at which overspeed is no longer safe without a steep deceleration afterwards.

Example 8.3 (Effect of a few cars underspeed in an otherwise uniform car train traveling at $v = v^D(u)$ is persistent). This time, we change the initial data (7.1) to

$$(u,v)(x,0) = \begin{cases} (u_1, v_1) = ① & \text{if } x < -1, \\ (u_2, v_2) = ② & \text{if } -1 \le x \le 0, \\ (u_1, v_1) = ① & \text{if } x > 0, \end{cases} \tag{8.2}$$

where both ① and ② are on $v = v^D(u)$; see Fig. 18. For such initial data, LWR model's solution will eliminate the (u_1, v_1) region in a finite time: the jumps at $x = -1$ and $x = 0$ are solved by a shock wave from ① to ② and by a rarefaction wave ② to ①, which necessarily interact and then annihilate.

The solution of (3.2) with initial data (8.2) is depicted in Fig. 18. Notice that in our model the shock from $x = -1$ and the rarefaction from $x = 0$ *do not interact*, differently from the corresponding solution of the LWR model. The solution has an expanding slower v_2-region moving upstream.

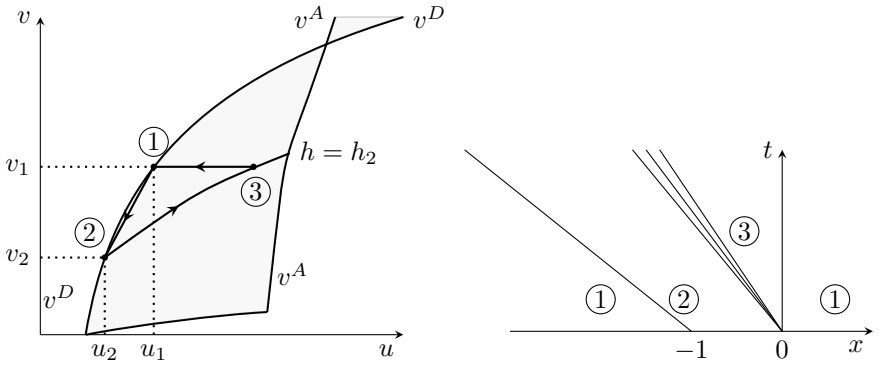

Fig. 18. A few cars underspeed in an otherwise uniform car train traveling at $v = v^D(u)$ can create a persistent slower region.

Example 8.4 (Over-braking Riemann solutions (6.4) can create phantom jams). Reconsider Example 8.2 using "'irrational" Riemann solutions (6.4). This way we can compare the effect of "rational" Riemann solvers vs. "irrational" ones.

Although we call the Riemann solution (6.4) "irrational", it is used when driver brakes hard for whatever reasons. So we also call (6.4) over-braking Riemann solution.

The initial value problem with data (7.1) solved using Riemann solution (6.4) is shown in Fig. 19 on the right. The Riemann solution used for the Riemann problem at $x = -1$ is of the type (6.4). Notice that the two shock waves on the left do

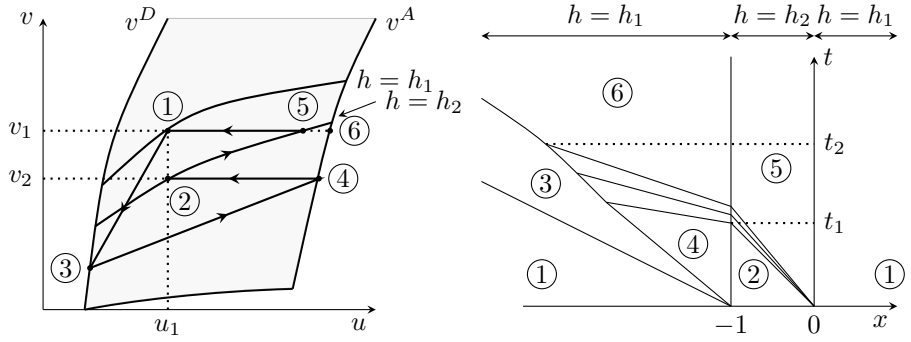

Fig. 19. Example 8.2 re-done using over-braking in the Riemann solution (6.4).

not interact. After waves finish their interactions in a finite time, the car platoon exhibits a phantom jam region ③ moving backwards along the car platoon, while the rest of cars travel at the higher speed v_1.

On a closed loop road, similar reasonings as in Example 7.3 show that the solution for t large enough has only two regions in which cars' speeds are slow (v_3) and fast (v_6), respectively. These two regions have stationary length and are moving upstream at the speed of the shock ③ $\xrightarrow{\text{ScAS}}$ ⑥, and this wave pattern becomes steady afterwards. This is again the stop-and-go wave pattern observed in Ref. 39.

Remark 8.2. The above examples reveal a possible mechanism to produce jams through small oscillations in speed in a car platoon traveling in congested zone $u < u_c$. Start at $t = 0$ from a uniform car train with constant spacing and speed $(\bar{u}, \bar{v})$ in the scanning zone, and the leading vehicle's speed is fixed at $\bar{v}$. Later, some drivers in the platoon drive temporarily and slightly above (or below) $\bar{v}$: they will make spacing more (or less) compact for themselves. If more drivers are biased to over-speed, then the car platoon become denser while the overall platoon speed is still $\bar{v}$. Once the spacing u decreases to $u = (v^D)^{-1}(\bar{v})$, over-speeding becomes impossible while under-speeding creates a persistent expanding slower car region upstream. Later, the same mechanism can repeat itself in the slower car region to create an even slower car region that is expanding upstream, causing jam eventually, unless upstream and/or downstream traffic spacing increase sufficiently.

Acknowledgment

The first author is a member of GNAMPA and acknowledges support from this institution. The research was partially supported by the PRIN 2015 project "Hyperbolic Systems of Conservation Laws and Fluid Dynamics: Analysis and Applications". The second author would like to thank NVIDIA Academic GPU Grant for contributing a Titan GPU enabling massive parallel computing on the GPU. The authors would like to thank the anonymous referee for many suggestions.

References

1. J. Almond, ed., *Proceedings of the Second Symposium on the Theory of Road Traffic Flow* (Organisation for economic co-operation and development, Paris, 1965).
2. S. Ahn, S. Vadlamani and J. Laval, A method to account for non-steady state conditions in measuring traffic hysteresis, *Transp. Res. B* **34** (2013) 138–147.
3. E. Andreotti, A. Bazzani, S. Rambaldi, N. Guglielmi, and P. Freguglia, Modeling traffic fluctuations and congestion on a road network, *Adv. Complex Syst.* **18** (2015) 1550009.
4. S. Blandin, J. Argote, A. M. Bayen, and D. A. Work, Phase transition model of non-stationary traffic flow: Definition, properties and solution method, *Transp. Res. B* **52** (2013) 31–55.
5. M. Blank, Hysteresis phenomenon in deterministic traffic flows, *J. Stat. Phys.* **120** (2005) 627–658.
6. M. Blank, Travelling with/against the flow. Deterministic diffusive driven systems, *J. Stat. Phys.*, **133** (2008) 773–796.
7. D. Chowdhury, L. Santen, and A. Schadschneider, Statistical physics of vehicular traffic and some related systems, *Phys. Rep.* **329** (2000) 199–329.
8. B. Coifman, Time space diagrams for thirteen shock waves, Technical Report, University of California (2018).
9. A. Corli and H. Fan, Two-phase flow in porous media with hysteresis, *J. Differential Equations*, **265** (2018) 1156–1190.
10. C. M. Dafermos, *Hyperbolic conservation laws in continuum physics* (Springer-Verlag, Berlin, 2016), 4th edition.
11. G. Dal Maso, P. G. LeFloch, and F. Murat, Definition and weak stability of nonconservative products, *J. Math. Pures Appl.* **74** (1995) 483–548.
12. H. Deng and H. Zhang, On traffic relaxation, anticipation, and hysteresis, *Transp. Res. Board* **2491** (2015) 90–97.
13. H. Fan and C.-W. Shu, Existence and computation of solutions of a model of traffic involving hysteresis, Preprint (2019).
14. M. Garavello and B. Piccoli, *Traffic flow on networks* (American Institute of Mathematical Sciences, 2006).
15. M. Garavello, K. Han, and B. Piccoli, *Models for vehicular traffic on networks* (American Institute of Mathematical Sciences, 2016).
16. F. L. Hall, B. L. Allen, and M. A. Gunter, Empirical analysis of freeway flow-density relationships, *Transp. Res. A* **20** (1987) 197–210.
17. D. Helbing, Traffic and related self-driven many-particle systems, *Rev. Mod. Phys.* **73** (2001) 1067–1141.
18. D. Helbing, H. J. Herrmann, M. Schreckenberg, and D. E. Wolf, eds., *Traffic and Granular Flow '99* (Springer, Berlin, 2000).
19. E. Isaacson and B. Temple, Nonlinear resonance in systems of conservation laws, *SIAM J. Appl. Math.* **52** (1992) 1260–1278.
20. E. Isaacson and B. Temple, Convergence of the 2×2 Godunov method for a general resonant nonlinear balance law, *SIAM J. Appl. Math.* **55** (1995) 625–640.
21. S. Kaufmann, B. Kerner, H. Rehborn, M. Koller and S. Klenov, Aerial observations of moving syncronized flow patterns in over-saturated city traffic, *Transp. Res. Part C* **86** (2018) 393–406.
22. B. Kerner, Phase transitions in traffic flow, in Helbing, Herrmann, Schreckenberg and Wolf, [18] pp. 253–283.
23. B. Kerner, Three-phase traffic theory and highway capacity, *Physica A* **333** (2004) 379–440.

24. R. A. Klausen and N. H. Risebro, Stability of conservation laws with discontinuous coefficients, *J. Differential Equations* **157** (1999) 41–60.
25. C. Klingenberg and N. H. Risebro, Convex conservation laws with discontinuous coefficients. Existence, uniqueness and asymptotic behavior, *Comm. Partial Differential Equations*, **20** (1995) 1959–1990.
26. W. Lam, S. Wong and H. Lo, eds., *Transportation and Traffic Theory 2009: Golden Jubilee* (Springer, Berlin, 2009).
27. J. A. Laval, Hysteresis in traffic flow revisited: An improved measurement method, *Transp. Res. B* **45** (2011) 385–391.
28. J. A. Laval and L. Leclercq, A mechanism to describe the formation and propagation of stop-and-go waves in congested freeway traffic, *Phil. Trans. R. Soc. A* **368** (2010) 4519–4541.
29. M. J. Lighthill and G. B. Whitham, On kinematic waves. II. A theory of traffic flow on long crowded roads, *Proc. Roy. Soc. London. Ser. A.* **229** (1955) 317–345.
30. W. K. Lyons, Conservation laws with sharp inhomogeneities, *Quart. Appl. Math.* **40** (1982/83) 385–393.
31. H. S. Mahmassani, ed., *Proceedings of the 16th International Symposium on Transportation and Traffic Theory* (Emerald Group Publishing Limited, 2005).
32. K. Nagel and P. Nelson, A critical comparison of the kinematic wave model with observational data, in Mahmassani, [31] pp. 145–163.
33. G. F. Newell, Theories of instability in dense highway traffic, *Oper. Res. Soc. Jap.* **5** (1962) 9–54.
34. G. F. Newell, Instability in dense highway traffic, a review, in Almond, [1] pp. 73–83.
35. P. I. Richards, Shock waves on the highway, *Oper. Res.* **4** (1956) 42–51.
36. M. Saifuzzaman, Z. Zheng, M. Haque and S. Washington, Understanding the mechanism of traffic hysteresis and traffic oscillations through changes in the task difficulty level, *Transp. Res. B* **105** (2017) 523–538.
37. B. Seibold, M. Flynn, A. Kasimov and R. Rosales, Constructing set-valued fundamental diagrams from jamiton solutions in second order traffic models, *Networks and Heter. Media* **8** (2016) 745–772.
38. R. Stern, S. Cui, M. L. Delle Monache, R. Bahdani, M. Bunting, M. Churchill, N. Hamilton, R. Haulcy, H. Pohlman, F. Wu, B. Piccoli, B. Seibold, J. Spoinkel and D. Work, Dissipation of stop-and-go waves via control of autonomous vehicles: Field experiments, *Transp. Res. Part C* **89** (2018) 205–221.
39. Y. Sugiyama, M. Fukui, M. Kikuchi, K. Hasebe, A. Nakayama, K. Nishinari, S. Tadaki and S. Yukawa, Traffic jams without bottlenecks experimental evidence for the physical mechanism of the formation of a jam, *New J. Phys.* **10** (2008) 033001.
40. B. Temple, Systems of conservation laws with invariant submanifolds, *Trans. Amer. Math. Soc.* **280** (1983) 781–795.
41. J. Treiterer and J. Myers, The hysteresis phenomenon in traffic flow, *Transp. Traffic Theory* **6** (1974) 13–38.
42. H. Yeo, Asymmetric microscopic driving behavior theory, Ph.D. Thesis, University of California, dec 2008.
43. H. Yeo and A. Skabardonis, Understanding stop-and-go traffic in view of asymmetric traffic theory, in Lam, Wong and Lo,[26] pp. 99–115.
44. K. Yuan, V. L. Knoop and S. P. Hoogendoorn, Capacity drop: Relationship between speed in congestion and the queue discharge rate, *Transp. Res. Board* **2491** (2015) 72–80.
45. H. M. Zhang, A mathematical theory of traffic hysteresis, *Transp. Res. B* **33** (1999) 1–23.